Spring 5-14-2022

TRANSISTION METAL CHALCOGENIDES AND PHOSPHIDES FOR ENERGY STORAGE AND CONVERSION THROUGH WATER SPLITTING

Kelsey Thompson
Pittsburg State University, kelsey.thompson@gus.pittstate.edu

Recommended Citation

Thompson, Kelsey, "TRANSISTION METAL CHALCOGENIDES AND PHOSPHIDES FOR ENERGY STORAGE AND CONVERSION THROUGH WATER SPLITTING" (2022). *Electronic Theses & Dissertations*. 396.
https://digitalcommons.pittstate.edu/etd/396

TRANSISTION METAL CHALCOGENIDES AND PHOSPHIDES FOR ENERGY STORAGE AND CONVERSION THROUGH WATER SPLITTING

A Thesis Submitted to the Graduate School
in Partial Fulfillment of the Requirements
for the Degree of
Master of Science

Kelsey Thompson

Pittsburg State University

Pittsburg, Kansas

May 2022

TRANSISTION METAL CHALCOGENIDES AND PHOSPHIDES FOR ENERGY STORAGE AND CONVERSION THROUGH WATER SPLITTING

Kelsey Thompson

APPROVED:

Thesis Advisor ______________________________
Dr. Ram Gupta, Department of Chemistry

Committee Member ______________________________
Dr. Khamis Siam, Department of Chemistry

Committee Member ______________________________
Dr. Serif Uran, Department of Physics

Acknowledgements

I would like to thank the many individuals who have helped in the prepartion and review of this work. Dr. Ram Gupta has been an important mentor and guide in providing technical support as well as lab space. His wealth of knowledge and expertise has been invaluable. Dr. Serif Uran and Dr. Khamis Siam are also due thanks for their support as members of the thesis committee as well as for their support as professors and their willingness to be available to answer questions provide explanations. Dr. Sanjay Mishra and his lab performed the SEM and XPS data recording. Wang Lin also deserves credit for assisting with the set up of equipment and the testing of materials.

I would also be remiss to ignore the finanical and moral support from my parents, siblings, and fiancé. Without the support of my parents I would not have been able to return to school and pursue this degree. And finally I want to acknowledge God for ultimately being the one who provides all things, including the ability to learn and understand. Soli Deo Gloria.

TRANSISTION METAL CHALCOGENIDES AND PHOSPHIDES FOR ENERGY STORAGE AND CONVERSION THROUGH WATER SPLITTING

An Abstract of the Thesis by
Kelsey Thompson

In contemporary society, there are many different ways that energy is used in daily life. From applications that require a high energy density to long-term storage in a stable manner, the requirements for energy usage are diverse. Therefore, the greater the number of uses a designed material exhibits, the more practical it may be for wide-scale manufacture. Two areas of particular interest for energy applications are fuel cells (to generate energy) and supercapacitors (to store energy). To provide cheaper and more durable alternatives for energy storage, electrodes containing $CoMoO_4$, $NiMoO_4$, $CoMoS_4$, $NiMoS_4$, CoMoP, and NIMoP were synthesized. The electrodes were synthesized through a hydrothermal method using Ni-foam as the substrate then tested as electrocatalysts for water splitting and electrodes for supercapacitor. As an electrocatalyst for hydrogen evolution reaction, $NiMoS_4$ displayed the lowest overpotential of 148 mV with a Tafel slope of 159 mV/dec. On the other hand, $CoMoS_4$ showed the lowest overpotential of 189 mV with a Tafel slope of 78 mV/dec among all four samples for oxygen evolution reactions. In terms of energy storage, the $CoMoO_4$ had the highest specific capacitance of 2652 F/g at a current density of 0.5 A/g with an averaged charge retention of 91% and a Coulombic efficiency of 99% after 10,000 cycles.

TABLE OF CONTENTS

LIST OF TABLES

TABLE PAGE

LIST OF FIGURES

CHAPTER I

INTRODUCTION

1.1 Rising Energy Demands

With the current population and economic expansion the demand for energy has begun to increase again after the decreased energy demand of the lockdown environment[1, 2]. The strain that was felt on natural resources used for energy has already begun to increase again. As was evident during the 2021 polar vortex that brought record low temperatures to much of the northern hemisphere, the current mixture of natural resources and renewables, such as solar and wind energy are not enough to combat such extreme events. With further future extreme cold weather events predicted in the future [3, 4], the need to continue the diversification of energy storage and conversion methods is crucial.

1.2 Meeting the Energy Need

Currently renewable energy sources are intermittent and rely on battery storage farms to even out the delivery of the energy they collect and convert to electricity. However a fast discharging system is needed to meet peak demand times to avoid problems such as rolling brown-outs as are currently experienced across California. Capacitors are known to discharge their stored energy very rapidly, but are limited in the amount of charge they can store on the surface between their plates. An alternative option for energy storage is the supercapacitor, which is a hybid device that can store charge through a chemical redox reaction like a battery and on plates (electrodes) like a capacitor. Supercapacitors provide an advantage over conventional batteries since they can discharge the energy they store much more quickly. They can also contain more power density, be made of less harmful materials, and typically have a longer life cycle than batteries or capacitors [5]. The challenges of replacing batteries with supercapacitors lie in their low energy density and energy storage stability due to current leakage. Devising an improved material out of which to manufacture supercapacitors must focus on these weaknesses and seek ways to improve them.

On the other hand, hydrogen generation through electrolysis presents many advantages for long-term energy storage. The challenges of hydrogen generation from water mainly present themselves in the form of energy efficiency. The thermodynamics of the reaction makes energy conversion inefficient, which also drives down cost-effectiveness. The other cost issue comes into play with the electrode materials, as platinum is currently the standard in hydrogen production. Platinum (Pt) is a rare and costly metal, which makes it a poor choice for large-scale industrial applications. Finding a more cost-effective electrode material that provides close to the same hydrogen yield as to what Pt electrodes can generate would be a good outcome. A comparison of the energy and power densities of conventional energy storage methods and newer storage methods can be seen in Figure 1.

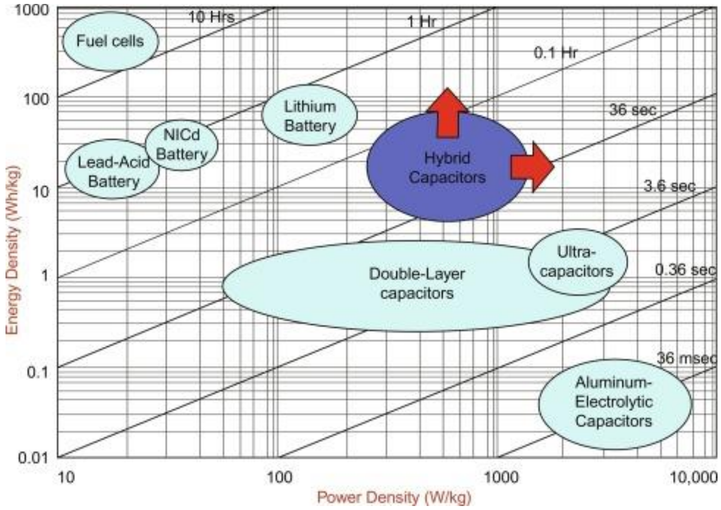

Figure 1: Ragone plot comparison of various energy storage devices. [6] Copyright 2021, Elsevier Inc.

The main goal of much of the current body of supercapacitor research involves finding ways to improve the energy density of a supercapacitor in a scalable and cost-effective way. Incidentally, many supercapacitor materials can also be used for electrocatalytic hydrogen and oxygen evolution reactions (HER and OER) [7–12]. Therefore, finding materials with double functions is of great interest. This poses a set of challenges centering around the oxygen evolution reaction, with its somewhat high reaction potential [13]. Noble metals and noble metal oxides, such as Pt and ruthenium oxide (RuO_2), are now used in commercial electrodes. For a variety of reasons, including cost, these electrode materials must be changed for future mass manufacturing. Due to their scarcity, these rarer metals have a high cost, which also implies that there isn't enough material to make a large number of devices incorporating these metals. Because materials like Pt and RuO_2 may be damaging to the environment and hazardous to humans, disposing of devices once they've served their purpose presents a new challenge.

1.3 Reasoning for Materials Selected

Less hazardous transition metal-based materials (Co, Ni, Fe, and Mo-based materials in particular), for charge storage applications and electrocatalytic reactions, have been the subject of the current trend in material research. For instance, several groups have worked with Co, Ni-Mo, and thiomolybdates and prepared them using various strategies. Using a sol-gel technique, Shaheen et al. created a MoO_3-$NiMoO_4$ nanomaterial. Specific capacitances for this material were 171.3 F/g at 2 mV/s under cyclic voltammetry and 204 F/g at 0.5 A/g during galvanostatic charge-discharge tests [14]. Thiagarajan et al. synthesized nanofibers containing $NiMoO_4$ using a hydrothermal method, and the specific capacitances of these fibers were 510 F/g at 1 A/g [15]. Liu et al. and Yang et al., on the other hand, used alternative ways to create $CoMoO_4$-$NiMoO_4$ nanostructures, including a coprecipitation approach and a hydrothermal procedure with subsequent annealing. These two groups had substantially higher specific capacitances, with 1039 F/g (at 2.5 mA/cm^2) and 751 F/g (at 1 A/g), respectively [16, 17]. However, these results are not very impressive, which can be attributed to insufficient intrinsic features of the binary transition metals pairs, Co-Mo and Ni-Mo.

Many recent studies have been undertaken to replace Pt and iridium oxide (IrO_2) electrodes that focus on more common transition metals like Fe, Co, Ni, and Zn [10, 14, 18]. Some approaches have sought to test samples based on the nonmetal with which the transition metal is conjugated, i.e., oxides, sulfides, selenides, and phosphides [7, 8, 19–21]. Other approaches have focused on using graphene oxides, composites, and various conducting polymers [22, 23]. In all of these approaches, the focus and challenge are to synthesize a material that has improved electrochemical properties for energy applications and can also act as a bifunctional electrocatalyst in both hydrogen and oxygen evolution capacities.

To regulate the electronic structure of Co-Mo and Ni-Mo-based materials, their incorporation with non-metallic elements (such as O, P, S, and Se) can be considered an efficient strategy to improve their electrochemical performance. Among various materials, transition metal phosphides (TMPs) have been found as possible catalysts for electrocatalysis and good materials for supercapacitors due to their excellent thermal stability and wide range of potential windows. Moreover, P has a lower electronegativity than O and S, and it has the optimum size for creating transition metal phosphides, making it a superior candidate for exceptional material designs. Furthermore, since P is negatively charged, it tends to trap and function as a site for positively charged ions, such as H_2 dissociation, while metal, being electropositive, prefers lone pair-containing species to trap and operate as active sites. Therefore, the incorporation of P into bimetal-based materials can probably show bi-functional HER and OER performance along with improved charge storage capabilities in supercapacitors [7, 8, 14, 18–22].

Several different groups have done work with cobalt and nickel molybdates and thiomolybdates that were synthesized through various methods. Thiagarajan et al. synthesized different nanofiber $NiMoO_4$ composites than Shaheen et al. using a hydrothermal method with obtained specific capacitances of 203 F/g, and 510 F/g at 1 A/g [15]. However, Liu et al. and Yang et al. both synthesized nanostructures of $CoMoO_4$-$NiMoO_4$ via a coprecipitation method and hydrothermally with subsequent annealing, respectively [16, 17]. These two groups reported much higher specific capacitances of 1039 F/g (at 2.5 mA/cm^2) and 751 F/g (at 1 A/g), respectively. Guo et al. also used a precipitation method to synthesize $CoMoS_4$ nanoflowers for use in lithium batteries with limited success in capacity during charge cycling but still had much clearer nanoflower morphology than other sulfide-containing samples [24]. Finally, Shao et al. tested $CoMoS_4/NiMoS_4$ composite materials as electrocatalysts that were synthesized from a one-step reaction method with overpotentials measured at 10 mA/cm^2 ranging from 78 – 191 mV [25].

To meet the challenges mentioned above, these metal oxides were chosen as potential electrodes for three main reasons, cost, durability, and environmental impact. Co and Ni materials are much cheaper than Pt, Co is also often used in drill bits for heavy materials because of its longevity, and neither Co nor Ni are heavy metals which can also be used as electrocatalysts. Aside from Co and Ni's structural advantages over other conventional electrode materials, these transition metals are cheaper and more abundant than Pt [26]. These metal oxides can also be used as capacitors/hydrolysis electrodes in conjunction with low concentration anion solutions instead of harmful and high concentration acidic solutions [27]. This makes them safer to handle and dispose of after they have reached the end of their lifecycle.

1.4 Objective of the Work

Based on the above concerns, the materials of $CoMoO_4$, $NiMoO_4$, $CoMoS_4$, and $NiMoS_4$, CoMoP, and NiMoP were selected and then successfully fabricated by coating Ni-foam using a hydrothermal method and then subsequently sulfurizing or phosphorizing in a tube furnace under an inert atmosphere. The sample surface composition was characterized via SEM, XPS, and XRD survey to verify their formation. Furthermore, these materials were tested for supercapacitor, HER, and OER efficacy. The results suggest that

$CoMoO_4$, $NiMoO_4$, $CoMoS_4$, $NiMoS_4$, CoMoP, and NiMoP show great potential for both supercapacitor and hydrolysis applications.

CHAPTER II

EXPERIMENTAL DETAILS

2.1 Materials

The chemicals used to synthesize the metal oxide precursors are as follows: $Co(NO_3)_2·6H_2O$ 99% and $Ni(NO_3)_2·6H_2O$ 99% from Strem Chemicals, Newburyport, Massachusetts, $Na_2MoO_4·2H_2O$ 99% from Sigma Aldrich, St. Louis, Missouri, and PVP, MW 1,300,000, K85-95. The sulfur source was obtained from $Na_2S·9H_2O$, extra pure from Acros Organics, USA. The phosphorus source for the samples was $H_2NaPO_2·H_2O$ 99% from Aldrich, Milwaukee, Wisconsin, USA. The nickel foam was procured from MTI-KJ Group, Richmond, California and cleaned before use. All chemicals were used as received from the company.

2.2 Synthesis of Electrode Materials

All nanostructured materials were synthesized using a hydrothermal method in the flat bottom, 40 mL Teflon reactors. The materials were synthesized on Ni-foam having an area of approximately 2 cm × 2 cm. Before deposition, the Ni-foam was pre-cleaned in a dilute HCl solution via ultrasonication for several minutes and then rinsed with distilled water and then ethanol. The $CoMoO_4$ was synthesized by dissolving equimolar (1.5 mmol) amounts of $Co(NO_3)_2·6H_2O$ and $Na_2MoO_4·2H_2O$ in 10 mL of distilled water. The mixture was then added to the PVP solution (300 mg of PVP in 20 mL of distilled water) and stirred.

Then the Ni-foam and solution were placed in the reactor, and the mixture was kept in an oven at 150 °C for 6 h. After the sample had cooled to room temperature it was rinsed with distilled water and dried. Finally, the sample was calcined at 350 °C for 2 h at 5 °C/min. This same procedure was repeated for the synthesis of $NiMoO_4$ with the exception that $Ni(NO_3)_2{\cdot}6H_2O$ was used instead of $Co(NO_3)_2{\cdot}6H_2O$ as one of the reactants. This procedure was repeated twice again without calcination for both the Ni and Co containing.

One each of the uncalcined synthesized oxide samples were converted from to sulfides through a solvothermal process. For this, a previously oxide-coated Ni-foam (uncalcined) was immersed in a 0.3 M Na_2S solution (20 mL) and transferred to a hydrothermal reactor (40 mL capacity), and heated to 140 °C for 24 h. After cooling to room temperature, the resulting electrodes were washed with DI water and dried at 60 °C under vacuum for 24 h before characterization and testing.

In the phosphorization process a one to five ratio of hydrothermally deposited mass to phosphorus was used to measure out the required amount of $H_2NaPO_2{\cdot}H_2O$. The nickel foam with the deposited $CoMoO_4$ was treated with phosphorus by placing it in a ceramic boat and the $H_2NaPO_2{\cdot}H_2O$ in a second ceramic boat. Both of these ceramic boats were placed in the tube furnace with the boat containing the $H_2NaPO_2{\cdot}H_2O$ placed nearest the Argon (Ar) gas source, toward the back half of the tube furnace. The tube furnace was set to reach a temperature of 320 °C from room temperature at a rate of 5 °C/min and to remain at that temperature for 2 h. After the sample had cooled back to room temperature it was examined and it was noted that the purple color of the $CoMoO_4$ was still evident, indicating that the phosphorization process was not complete. Therefore the process was repeated a second time with a newly measured amount of $H_2NaPO_2{\cdot}H_2O$. After the second time in the tube furnace the sample came out with the characteristic black color all over the sample and no purple color from the Co sample still evident. Due to this result the nickel sample was placed in the tube furnace with a 1 to 10 ratio of phosphorus instead of the 1 to 5 ratio used initially. The result was that the nickel foam had a more complete phosphorization initially. These square pieces of nickel foam were then cut into three equal sized strips to be used for testing.

2.3 Structural Characterization

The synthesized samples were structurally characterized using scanning electron microscopy (SEM), X-ray diffraction (XRD), and X-ray photoelectron spectroscopy (XPS).

2.3.1 Scanning Electron Microscopy

Scanning electron microscopes operate by generating an electron beam at the cathode and accelerating it past an anode. The elctron beam is further condensed as it is directed towards the sample to be analyzed. The energy of the electron in the beam that impinges on the sample determines how it interacts with the sample through inelastic collsions. Higher energy electrons can penetrate more deeply into the sample and can cause X-rays to be released from the deeper regions of the sample, within approximately 1 micrometer, of the sample. The surface morphology of the sample is imaged through the reflection and released of secondary electrons from the sample. These secondary electrons have lower energy, higher intensity, and are therefore more easily detected. The detector amplifies the signal so that it can be visualized and the surface morphology of the sample can be seen. This work’s samples microstructural properties were investigated using a Quanta 200 SEM (FEI, Hillsboro, Oregon, USA).

2.3.2 X-Ray Photoelectron Spectroscopy

X-ray photelectron spectroscopy is used to determine the identity of elements as well as how they are bonded together in the surface layer of a sample. The peak positions of the individual element and the bonded element can be compared since the electrons analyzed in an XPS survey are the inner electrons. The shifts in the valence electrons from bonding affect the innner electrons energy levels. The shift in the bonding energy peaks seen is determined by the other element that the element to be analyzed is bonded to. This is because the interactions of the electron cloud with the bonded atom repel the inner electrons of the atom being studied. This causes the inner electrons to be closer to the nuclues and therefore are more tightly bound, thus increasing the binding energy slightly. The amount of binding energy changes depending on the elements in question and how they are bonded, for example, the Mo-O bond and the Mo-S bond cause the inner electrons to have different binding energies. An example of this in bulk Mo and quantum dot Mo as can be clearly seen in Figure 2 [28]. As can clearly be seen when comparing the Mo 3d peaks as well as the S 2p peaks in the bulk to the quantum dots there is a definite shift in the binding energies when the bonding changes.

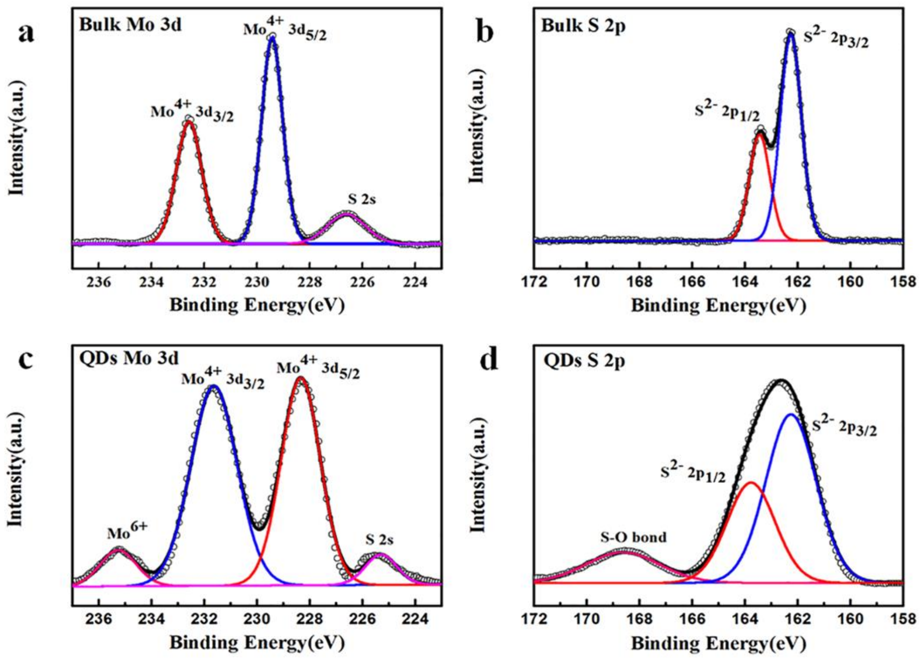

Figure 2: High-resolution XPS of Mo 3d [a], S 2p [b] spectra for bulk MoS_2, Mo 3d [c], and S 2p [d] for MoS_2 quantum dots. [28] Copyright 2017, The Author(s).

The synthesized samples' chemical composition was determined via XPS analysis using a ThermoFisher Scientific Instruments analyzer (East Grinstead, UK). A monochromatic Al K_α radiation source (hν = 1486.6 eV) and an X-ray spot size of ~400 μm in radius were used for data recording. The elemental survey spectra were recorded using a pass energy of 200 eV. Passing energy of 50 eV was used for recording high-resolution core-level spectra for all the elements. The Advantage software was used for the peak fittings.

2.3.3 X-Ray Diffraction Analysis

X-ray diffraction is used to analyze the crystal structure of a solid. A small amount of the powdered sample is placed on a slide and a X-ray beam is is then directed toward the sample. The sample or the beam are rotated through several different angles and the reflected beam is detected. The intenisty of the reflected beam is recorded and the resulting peaks are then compared to standards for the sample to determine the crystalline or amorphous nature of the sample. If the sample is highly crystalline in nature the indentity and purity of the sample can be confirmed through these comparisons. This is because Bragg's Law, seen in Equation 1, can be used to determine the h, k, & l, values of the crystal lattice from the $2\boldsymbol{\theta}$ values given by the XRD data,

$$n\lambda = 2d\sin\theta \qquad (2.1)$$

where n is the diffraction order, $\boldsymbol{\lambda}$ is the wavelength of the incident beam, d is the lattice constant, and $\boldsymbol{\theta}$ is the angle of relfection. If the resultant XRD pattern closely matches known patterns then the crystal structure then the purity of the sample is high. XRD patterns were recorded using a Shimadzu X-ray diffractometer (Lenexa, Kansas, USA). Cu $K_{\alpha 1}$ radiation (λ=1.5406 Å) in the 2θ-θ mode was used to study the crystallinity and phase purity of the synthesized samples.

2.4 Electrochemical Characterizations

All electrochemical characterizations were performed using a VersaSTAT 4-500 potentiostat, galvanostat electrochemical workstation (Princeton Applied Research, TN, USA) using a three-electrode system. The electrodes were tested for energy storage through cyclic voltammetry (CV), galvanostatic charge-discharge (CD), and electrochemical impedance spectroscopy (EIS) in a 3 M KOH solution.

2.4.1 Cyclic Voltammetry

Cyclic voltammetry tests are preformed to provide information of the energy storage capacity of an electrode material as shown in Equation 2.2,

$$C_{sp} = \frac{\int_{V1}^{V2} i * V * dV}{m * v * (V2 - V1)} \tag{2.2}$$

where V_1 and V_2 stand for the working potential limits (V), i stands for the current (A), m stands for the mass (g) of the electroactive materials, and v is the scan rate (mV/s). This is achieved through applying a set potential to the electrode system and measuring the responding current. The applied potential is increased at a set rate until the threshold has been reached. The potential range applied depends on the type of electrode material being tested. Too much potential applied to the sample can damage the materials so that the redox reaction no longer happens as effeectively. For transition metal oxides the voltage testing window is from 0 to 0.6 V. Then a new scan rate is selected and the potential is cycled through the window again and the current is measured. This process is repeated through all the chosen scan rates, for this work scan rates of 2, 5, 10, 20, 30, 50, 75, 100, 125, 150, 175, 200, 225, 250, 275, and 300 mV/s were selected.

When the potential and current density data are plotted the area inside the curve represents the amount of energy stored by the supercapacitor. The energy is stored through electron transfer via redox reaction. As the potential is increased from 0 V the oxidation process begins and electrons are removed from capacitive material. When the potential is eventually reversed the reduction process begins and the electrode materials are restored back to their original state. The shape of the CV curve can give information about how many oxidation states a transition metal chalconide contains through either a double peak or an elongated peak, which is more noticeable at lower scan rates than at higher scan rates.

2.4.2 Galvanostatic Charge-Discharge

Galvanostatic charge-discharge tests also provide information about he energy storage capabitility of the electrode material through charging the electrode to a set potenital at varying current densities. As the current is applied the change in voltage over time is recorded and then plotted. For trasition metal oxides and the peak voltage is set to 0.6 V to avoid damaging the sample through over charging it. The time it takes the sample to discharge its current is directly related to the energy stored in the sample as show by Equation 2.3,

$$C_{sp} = \frac{i * \Delta t}{\Delta V * m} \tag{2.3}$$

where *i* is the current density (A/g), Δt is the discharge time (s), ΔV is the potential range, and m is the mass of materials. Equations 2.4 & 2.5 are used to calculate the energy and power densities through the use of the collected time, potential, and current density data, which can then be graphed in a Ragone plot for easier comparison,

$$E = \frac{1}{2} C V^2 \tag{2.4}$$

$$P = \frac{E}{t} \tag{2.5}$$

where *C* is the specific capacitance of the active material, *V* is the cell potential, and *t* is the discharge time measured in seconds.

As the current density is applied to the sample the voltage increase can happen through two main mechanisms if the elecrode is made of a redox material. Typical redox electrode materials exhibit two main charging mechanisms. The initial charging happens rapidly, then as the redox reaction begins the curve flattens and then peaks. As the material discharges the redox reaction is reversed and then the electrolytic double layer is dissipated. The longer self discharge takes the better the material is suited for battery applications.

2.4.3 Cyclic Performance

Another important aspect of electrodes materials is their ability to be charged and discharged many times and still retain their level of energy density. Therefore each electrode material is taken through several charge/discharge cycles at a set current density and the time and potential data are recorded. The materials are cycled through several thousand cycles and then the first and last several cycles data are compared to each other. Snapshots of certain points are also collected and used to calculate the capacitance retention (Equation 2.6) and coulombic efficiency (Equation 2.7),

$$Capacitance\ Retention = \frac{C_{sp}}{C_{spi}} \times 100\% \qquad (2.6)$$

where C_{sp} is the capacitance at that cycle calculated using Eqn 2.2 and C_{spi} is the initial capacitance calculated after the first cycle. The capacitance is calculated every 500 cycles and then plotted with the coulombic efficiency. Coulombic efficiency is calculated using the charge and discharge times as shown in the following equation:

$$Coulombic\ Efficiency = \frac{t_4 - t_3}{t_2 - t_1} \times 100\% \qquad (2.7)$$

where t_3 and t_4 are the starting and ending times of the discharge cycle and t_1 and t_2 are the starting and ending times of the charging cycle. These results are plotted against the cycle to track how the sample performs over time.

If an electronic device with this energy storage system is assumed to go through one charge/discharge cycle per day then 5000 cycles could be considered to represent over 13 years of device “life.” As the electrode is charged and discharged it can be damaged over many cycles and the capacitance retention can decrease. This damage can also impact the time it takes the device to charge and affect the self discharge of the device.

2.5 Electrocatalytic Testing

All electrochemical characterizations were performed using a VersaSTAT 4-500 electrochemical workstation (Princeton Applied Research, TN, USA) using a three-electrode system. Electrocatalytic tests for hydrogen evolution reaction and oxygen evolution reaction activity, tests of linear sweep voltammetry (LSV), chronoamperometry (CA), and EIS were performed using a 1 M KOH solution.

2.5.1 Linear Sweep Voltammetry

Linear sweep voltammetry is performed during the hydrogen evolution and oxygen evolution reactions to determine at what current density the reaction will occur under determined applied voltages. For HER testing the voltage is applied from -0.4 V to 0.4 V and the resulting current densities are recorded. For OER testing the voltage is applied from 1.4 V to approximately 1.7 V and the current densities are recorded. The potential that is applied to reach 10 mA/cm^2 is used to determine the overpotential of the reaction. Since the reaction potential for the hydrogen reaction is defined at 0 V the overpotential is recorded at the value found at the 10 mA/cm^2. However since the reaction potential for the oxygen reaction is defined at 1.23 V the overpotential for the reaction is found by subtracting the defined value from the potential value recorded at 10 mA/cm^2.

The other important piece of information that can be determined from the LSV data is the reaction kinetics through plotting a Tafel slope. The log of the current density is plotted against the applied voltage and the middle portion of the curve is used to determine the reaction kinetics. A lower Tafel slope value indicates faster kinetics for the HER/OER, which means more gas production for the electrode material.

2.5.2 Electrochemical Impedance Spectroscopy

During electrochemical impedance spectroscopy the internal resistance of an electrode material is measured by applying a set voltage and the real and imaginary Z values are recorded and then plotted in a graph called a Nyquist Plot. The points along the curve of the Nyquist Plot prepresent the impedance at a specific frequency for that curves particular voltage. As the frequency of the applied voltage changes the imaginary impedance will typically increase and then decrease as the real portion of the impedance increases.

2.5.3 Chronoamperometry

Chronoamperometry is another way to test the stability of an electrode during OER/HER performance. Unlike with repeated LSV-CV tests, in CA tests the voltage is held constant and the OER/HER reaction is allowed to continue for 18 to 24 hours. The resulting current density is recorded over time to determine how well the electrode can withstand long term, continual use as compared to cyclic use. This test is important for applications where constant oxygen generation would be necessary such as in a wearable oxygen pump for a patient that needs some sort of mobile oxygen generating device.

CHAPTER III

RESULTS AND DISCUSSION

3.1. Structural C haracterization

3.1.1 SEM

Figure 3 details the scanning electron microscope images of the oxide and sulfide samples. The image of $CoMoO_4$ (Figure 3a) indicates the formation of nanosheets sprouting from nanoflower centers. The nanoflowers made of the sheets are microsize in diameter and show an increase in surface area compared to flat nanosheets. The nanoflowers are not arranged uniformly across the nickel foam but grow from conglomeration points into larger bunches. SEM images of the $NiMoO_4$ (Figure 3b) show strand or wire shapes, approximately 4 μm long with nanothicknesses of less than 100 nm, forming a web-like pattern. The wires bundle in a few areas but are mostly spread out to offer a large, highly porous surface area. The coating of the Ni materials was uniform over the nickel foam substrate, unlike the Co-containing materials. Both sulfide-containing samples (Figure 3c-d) display an increase in density as the nanoflower sheets and nanowires have much less space in between the structures. This increase in density can be attributed to the difference in atomic radii between sulfur and oxygen.

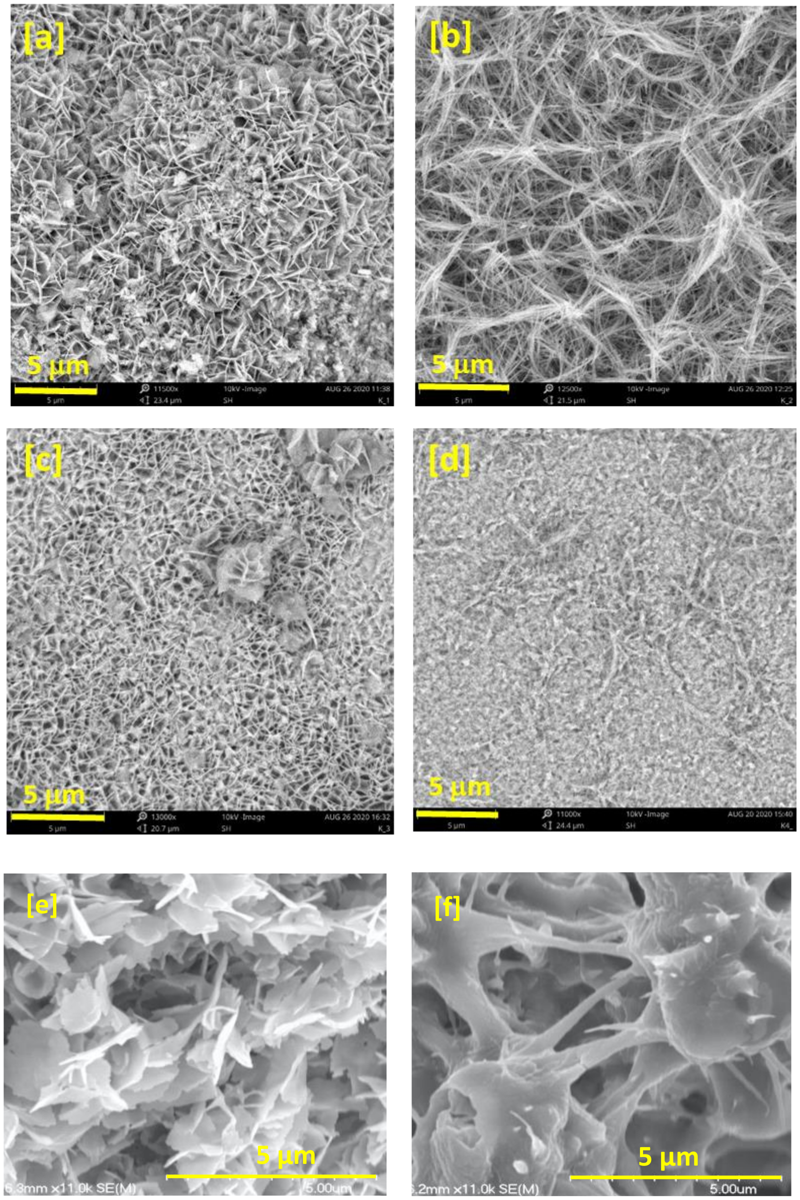

Figure 3: SEM images of [a] $CoMoO_4$, [b] $NiMoO_4$, [c] $CoMoS_4$, [d] $NiMoS_4$, [e] CoMoP, and [f] NiMoP samples.

The SEM technique was also used to examine the morphology of the prepared CoMoP and NiMoP samples. As illustrated in Figure 4a, SEM images of the CoMoP sample revealed a nanoflower-like morphology. However, after collapsing inward on itself, it appears to include some amorphous unstructured patches (Figure 4b). This is likely owing to the phosphorization process because phosphorus is bigger than oxygen, and the resulting decrease in distance between the atoms might result in more interactions. Similarly, the NiMoP sample had some clumping at the nanowire’s morphology (Figure 4c-d) [9].

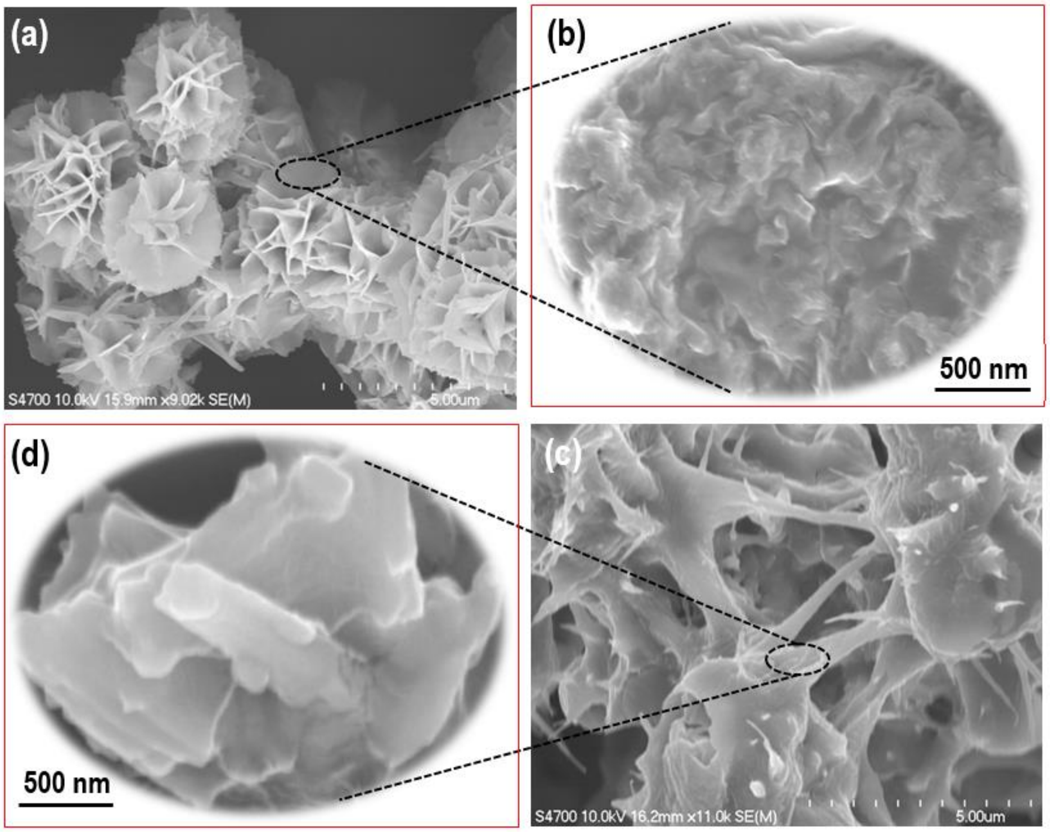

Figure 4: SEM images of (a) CoMoP catalyst, (b) enlarged CoMoP catalyst, (c) NiMoP catalyst, and (d) enlarged NiMoP catalyst.

3.1.2. XPS

All six samples were analyzed via a wide scan with X-ray photoelectron spectroscopy to characterize the synthesized materials' surface atoms. The wide scan XPS survey spectra are shown in Figure 5a. The wide scan survey spectra confirm the presence of expected elements in each sample. The high-resolution XPS spectra for each sample's elements of interest are contained in Figure 5b-i. In Figure 5b & f, the $CoMoO_4$ sample shows peaks for cobalt and oxygen bonding in the $2p_{1/2}$ and $2p_{3/2,}$ similar to that described by Tan et al., as well as a typical 1s peak for oxygen at 531.4 eV [29]. The values for the oxygen peaks shown in Figure 5f & g were very similar for all the samples suggesting that the oxygen in all the samples are bonded similarly when comparing the oxides, sulfides, and phosphides to each other. Figure 5d & e also shows peaks for molybdenum at the $3d_{5/2}$ [30] and $3d_{3/2}$ [31] positions that are clearly defined. In Figure 5b the $CoMoS_4$ sample has slightly different peak values that are shifted to slightly lower values for the 2+ and 3+ oxidation states, and the sulfur $2p_{3/2}$ peak shown in Figure 5h is also close in value to the work of Alstrup et al. [32]. The $NiMoO_4$ peak, seen in Figure 5c, for nickel $2p_{3/2}$ also agrees with several other reported results as well [20, 30, 33]. The $NiMoS_4$ sample also has peak shifting shown in Figure 5c that is similar to what was seen in the $CoMoS_4$ sample with slightly lower peak values for the oxidized nickel. In Figure 5d & e the molybdenum peaks for both sulfur samples were spread farther apart and had a different arrangement of Gaussian peaks in the results as well, indicating that the sulfur-containing samples exhibit slightly different bonding than the oxide compounds [34, 35].

According to the XPS elemental studies for the phosphide samples, the element ratio in oxide samples was 1:1:4 with the compositional formula $MMoO_4$ (M=Co, Ni), but the element ratio in phosphide samples was 1:1:1 with the compositional formula MMoP (M=Co, Ni). The high-resolution XPS spectrum of Co 2p is shown in Figure 5b. The split-spin orbit Co $2p_{3/2}$ and Co $2p_{1/2}$ components, as well as the associated satellite peaks, were de-convoluted from the Co 2p spectrum. The binding energies in the Co $2p_{3/2}$ area were assigned to the Co-O (781.8 and 797.8 eV), Co-P (778.4 and 793.2 eV), and oxidized Co kinds (781.4 eV). Binding energies of 792.9, 798.4, and 802.0 eV can likewise be attributed to Co-P and oxidized Co types in the Co $2p_{1/2}$ area. The high-resolution Mo 3*d* spectra of CoMoP (Figure 5d) exhibit two peaks at 228.5 and 231.8 eV, which may be ascribed to Mo $3d_{5/2}$ and Mo $3d_{3/2}$, respectively, and are higher than the metallic MoO (227.6 eV) species, which can be assigned to Mo^{+} species [17]. The peaks at 230.2, 233.3, and 235.5 eV can be attributed to oxidized Mo species; they may have resulted from surface oxidation of CoMoP. Meanwhile, the high-resolution XPS of the P 2*p* core level showed these peaks at 129.3 and 129.8 eV, which were assigned to the binding energies for P $2p_{3/2}$ and P $2p_{1/2}$ of P-Co, respectively (Figure 5f). And the strong peak located at 134.1 eV belonged to the P-O species. Previous reports had explained that the P-O signal arose from the inevitable surface oxidation after the exposure of metal phosphide to air. Similar, XPS results appeared for the NiMoP sample, as shown in Figure 5c, e, g, & i.

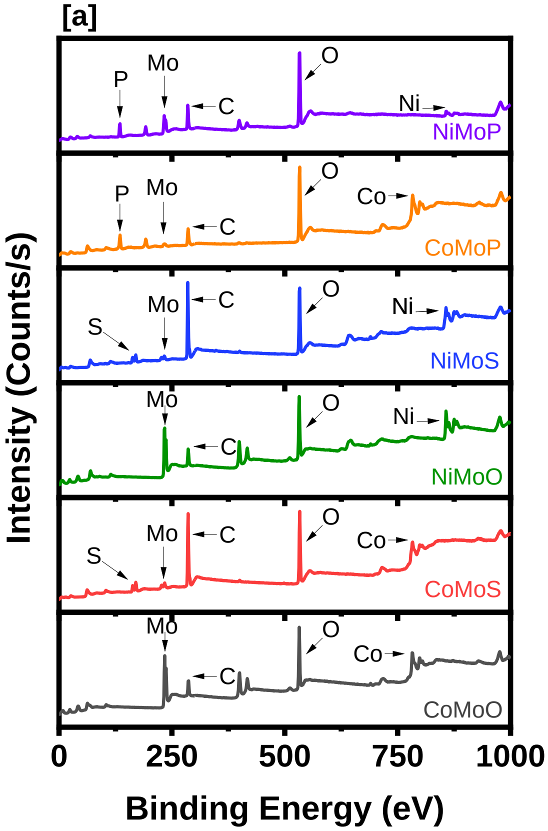

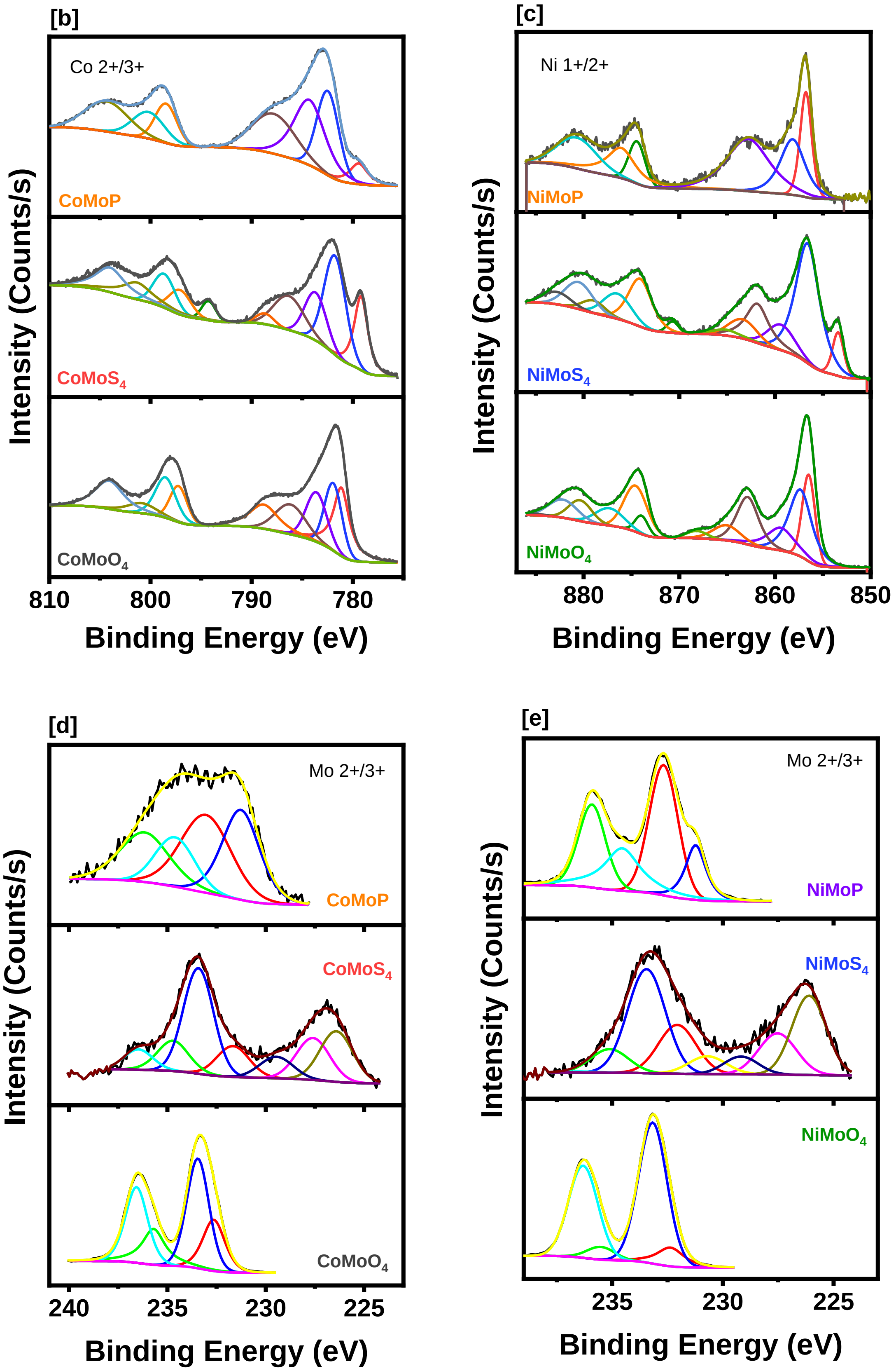
[b]
Co 2+/3+
CoMoP
CoMoS4
CoMoO4
810
800
790
780
Binding Energy (eV)
Intensity (Counts/s)
[c]
Ni 1+/2+
NiMoP
NiMoS4
NiMoO4
880
870
860
850
Binding Energy (eV)
Intensity (Counts/s)
[d]
Mo 2+/3+
CoMoP
CoMoS4
CoMoO4
240
235
230
225
Binding Energy (eV)
Intensity (Counts/s)
[e]
Mo 2+/3+
NiMoP
NiMoS4
NiMoO4
235
230
225
Binding Energy (eV)
Intensity (Counts/s)

[f]

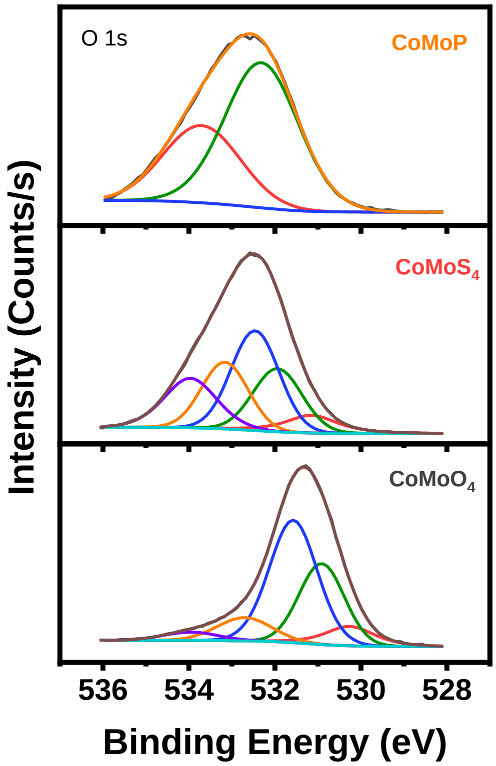
O 1s
CoMoP
CoMoS$_4$
CoMoO$_4$
Intensity (Counts/s)
536
534
532
530
528
Binding Energy (eV)

[g]

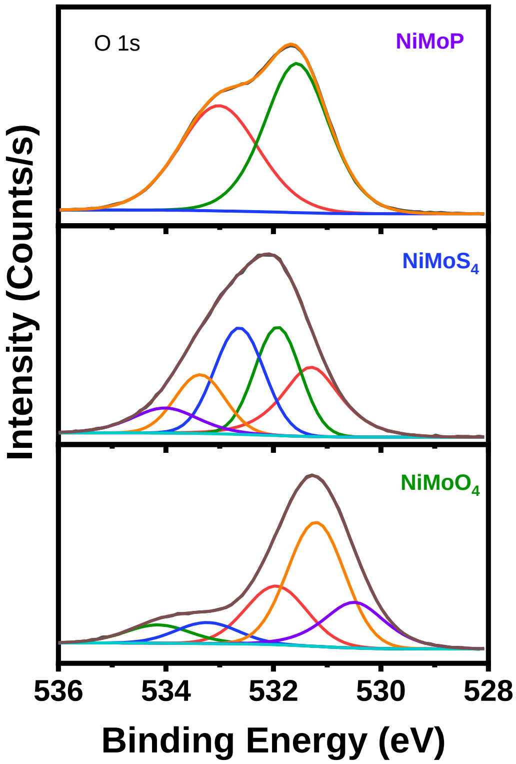
O 1s
NiMoP
NiMoS$_4$
NiMoO$_4$
Intensity (Counts/s)
536
534
532
530
528
Binding Energy (eV)

[h]

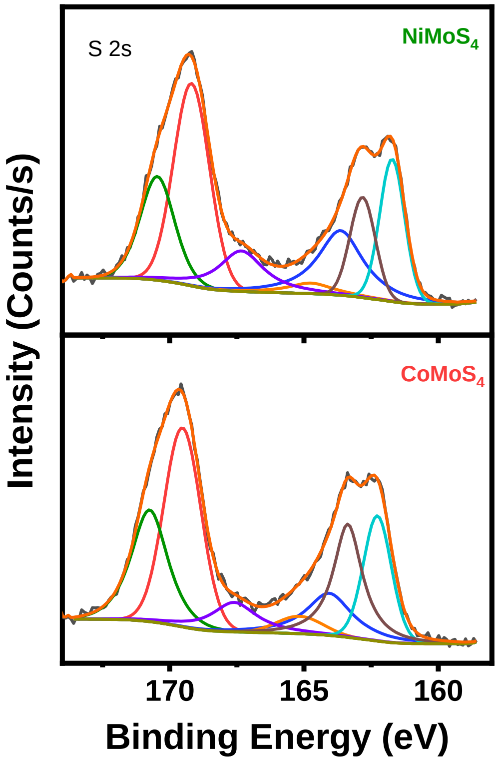
S 2s
NiMoS$_4$
CoMoS$_4$
Intensity (Counts/s)
170
165
160
Binding Energy (eV)

[i]

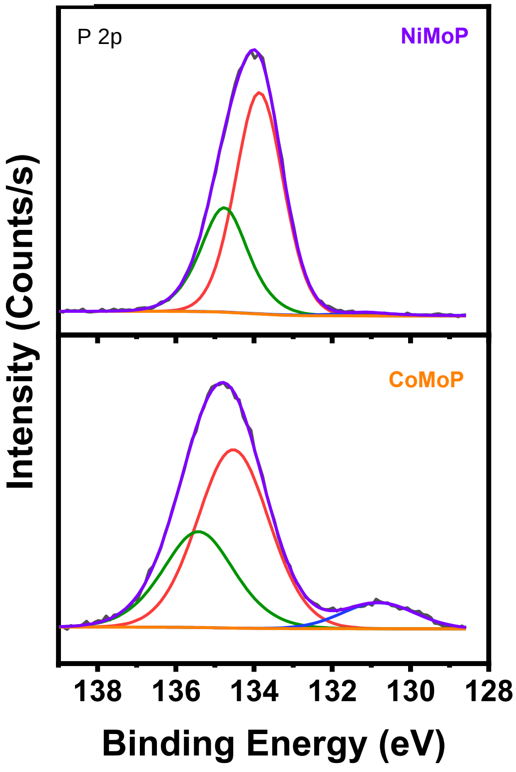
P 2p
NiMoP
CoMoP
Intensity (Counts/s)
138
136
134
132
130
128
Binding Energy (eV)

Figure 5: XPS plots: [a] wide range scan of all six samples, high resolution scans for [b] Co, [c] Ni, [d] Mo in the Co samples, [e] Mo in the Ni samples, [f] O in the Co samples, [g] O in the Ni samples, [h] S, and [i] P.

3.1.3. XRD

X-ray diffraction data for all samples are shown in Figure 6. $CoMoO_4$, $NiMoO_4$, and $NiMoS_4$ had limited clear peaks indicating the as synthesized materials' slightly crystalline nature as similar to other reported XRD data [24]. $NiMoO_4$ is known to be monoclinic in its crystal structure when forming nanorods, and the results of the synthesized sample closely match those reported by Yang. (JCPDS No. 13-0128) [36, 37]. Furthermore, Figure 6c, e, & f show the XRD pattern for $CoMoS_4$, CoMoP, and NiMoP, respectively, indicating their amorphous nature.

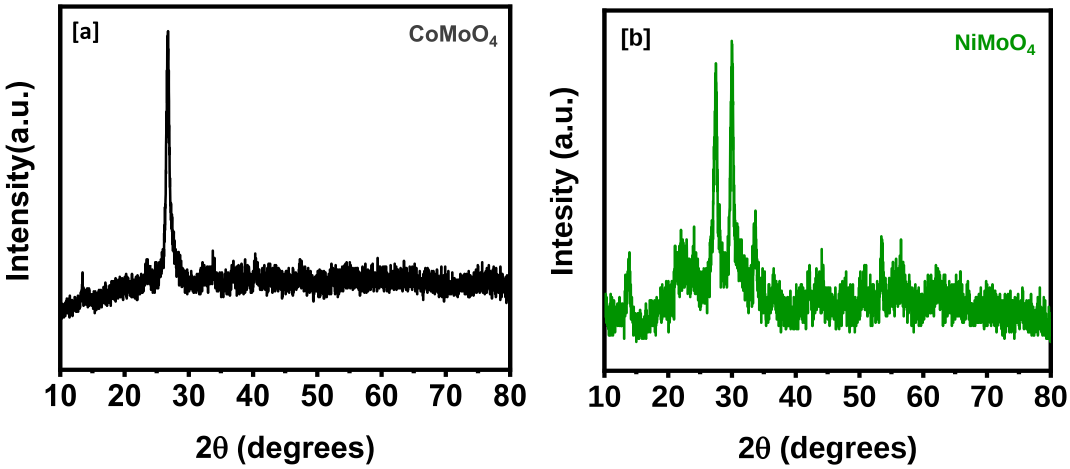

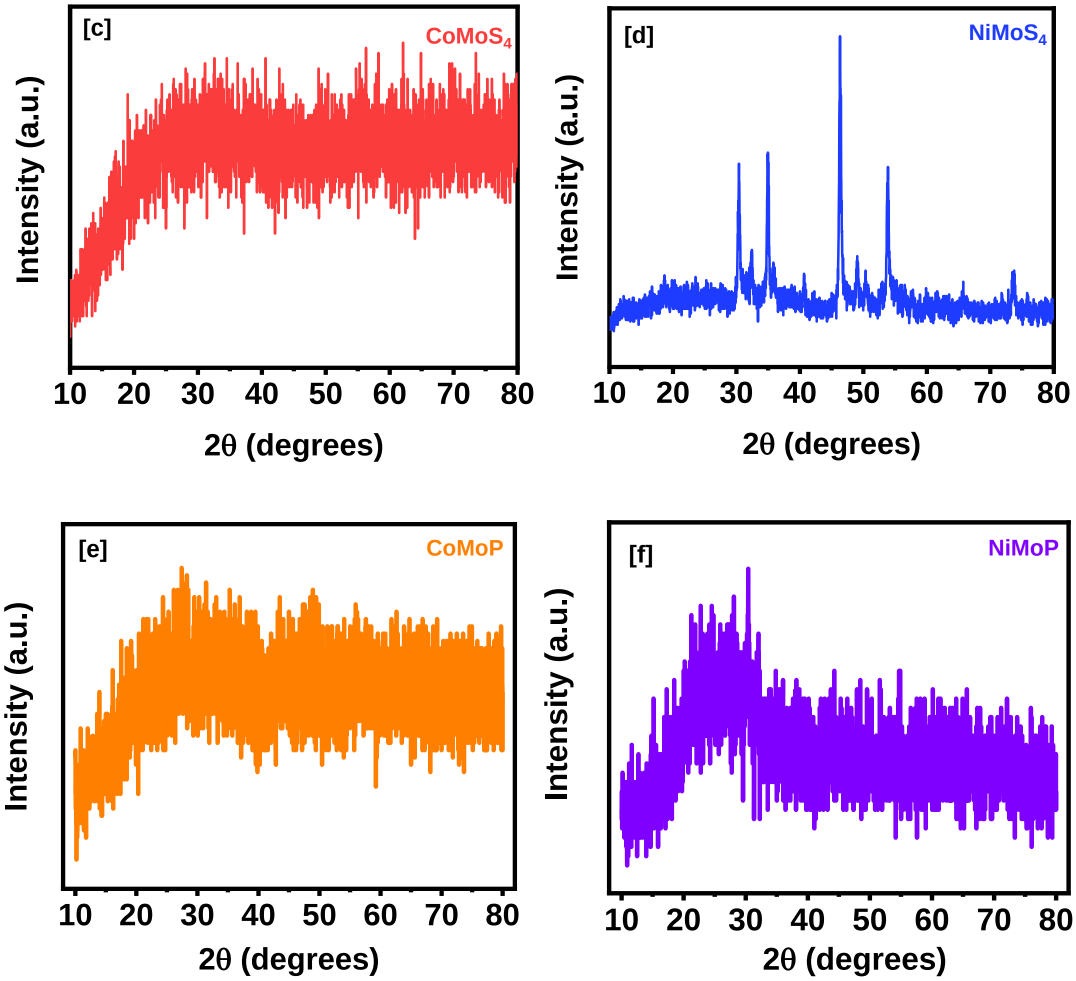

Figure 6: XRD patterns of [a] $CoMoO_4$, [b] $NiMoO_4$, [c] $CoMoS_4$, [d] $NiMoS_4$, [e] CoMoP, and [f] NiMoP.

In the XRD pattern of $NiMoS_4$, intrinsic peaks of $NiMoS_4$ material were detected as shown more clearly in Figure 7b, which was matched with reported Shao works (JCPDS No. 73-0574) [25]. Additionally, some peaks observed at the pattern of $NiMoO_4$ material were seen in Figure 7b. This indicates that $NiMoS_4$ was not completely sulfurized through hydrothermal reaction, and the $NiMoS_4$ contains some $NiMoO_4$ surface components.

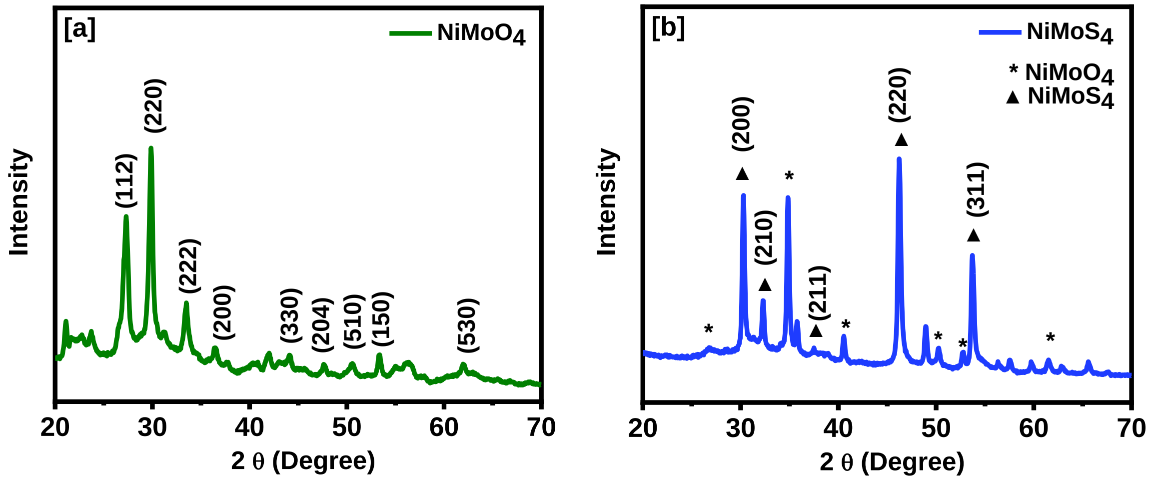

Figure 7: XRD patterns of [a] $NiMoO_4$, and [b] $NiMoS_4$.

3.2. *Electrochemical Characterization*

3.2.1. Supercapacitors

The six samples were tested for supercapacitor applications by collecting CV, CD, and EIS data. Figure 8 contains the cyclic voltammetry curves for the electrodes, which were collected from potentials of 0.0 to 0.6 V and scan rates of 2 to 300 mV/s. As seen in the figures, all samples exhibited asymmetrical CV curves, with peak separations varying for the electrode based on whether it contained Co or Ni. The presence of anodic and cathodic peaks and the asymmetric nature of the curves suggest that these electrode materials would function as pseudocapacitors.

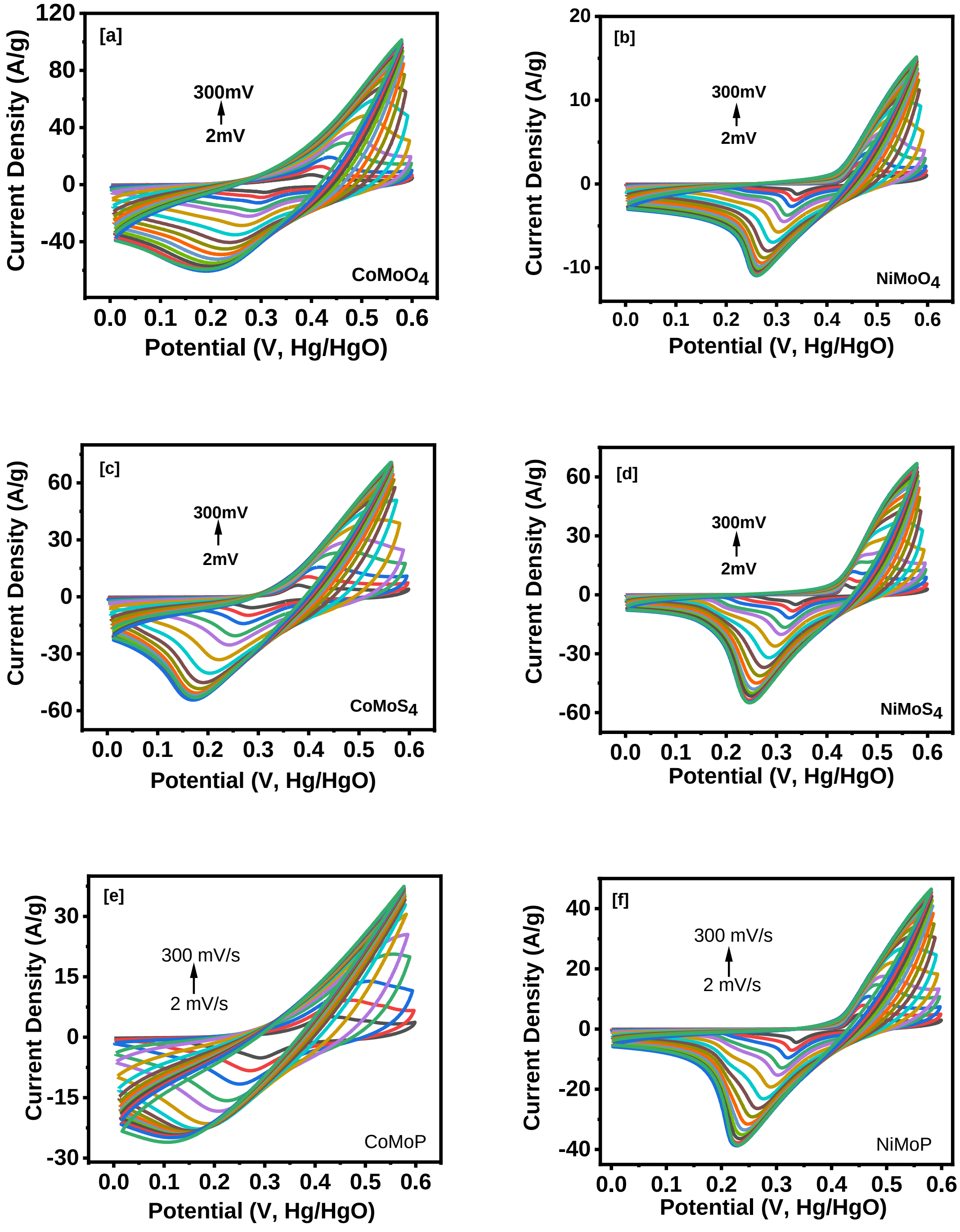

Figure 8: CV curves from scan rates of 2 mV/s to 300 mV/s of [a] $CoMoO_4$, [b] $NiMoO_4$, [c] $CoMoS_4$, [d] $NiMoS_4$, [e] CoMoP, and [f] NiMoP.

The CV data show that the cobalt samples begin the oxidation process on the electrode at lower potentials than the nickel samples. The $CoMoS_4$ sample shows a much higher current density for both the oxidation and reduction processes over the same potential differences as for the other samples. This means that the cobalt samples have a greater potential for energy storage than the nickel samples do. The larger values obtained from the difference in the anodic and cathodic peak currents agree with this observation, having values of 0.499, 0.125, 0.076, and 0.061 A/g for $CoMoO_4$, $CoMoS_4$, $NiMoO_4$, and $NiMoS_4$, respectively. The scan rate vs. specific capacitance graph (Figure 9a) also shows that the Co samples have a higher specific capacitance over all scan rates than the Ni samples. Since cobalt has two separate oxidation states of +2/+3, two different redox potentials are most noticeable at slower scan rates which causes the CV of cobalt samples to have a much different shape than that of a nickel CV with its one +2 oxidation state, giving it a much sharper redox peak than the cobalt. However, the NiMoP sample reached a higher current density than the CoMoP sample despite Ni having only one oxidation state. This discrepancy may be due to the molybdenum complex being more structured in the NiMoO state, as shown by the differences in the Mo XPS graphs for both samples. While the NiMoP was able to reach a greater current density at high scan rates, it does not follow that it had a much greater energy storage capacity.

The specific capacitance, C_{sp}, of the samples can be calculated as a function of the scan rate using Equation 3.1. The CV data was used in conjunction with the equation below to calculate the specific capacitance,

$$C_{sp} = \frac{\int_{V1}^{V2} i * V * dV}{m * v * (V2 - V1)} \tag{3.1}$$

where V_1 and V_2 stand for the working potential limits (V), i stands for the current (A), m stands for the mass (g) of the electroactive materials, and v is the scan rate (mV/s).

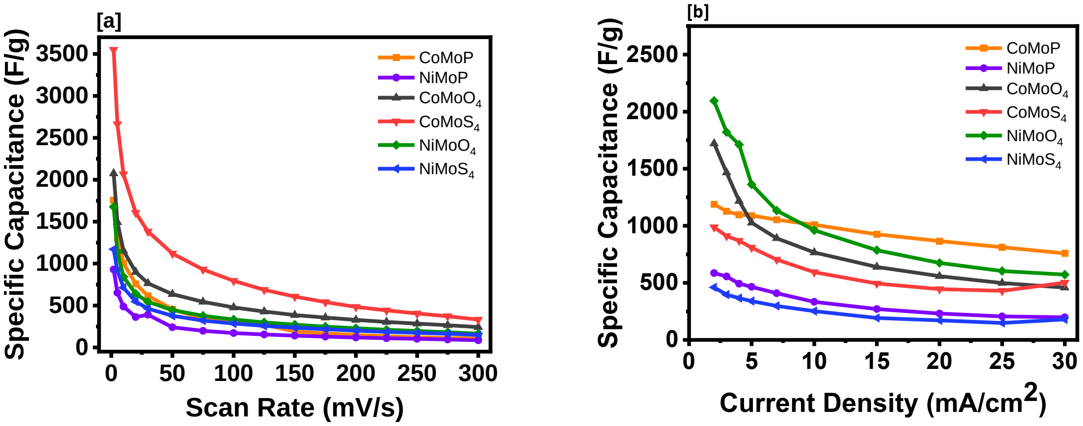

Figure 9: Variation of C_{sp} vs scan rate [a] and current density [b] for all six samples.

The galvanostatic charge-discharge tests were performed at various current densities of 1, 1.5, 2, 3, 4, 5, 7, 10, 15, 20, 25, and 30 mA/cm^2. As the current density was decreased, the samples reached saturation, and the peak voltage was reduced slightly so that the discharge cycle could be realized. The galvanostatic charge-discharge tests (Figure 10) for the samples yielded promising results, especially for the oxide samples. At a current density of 0.75 A/g, the discharge time for the $NiMoO_4$ sample was 1965 sec (~33 min), and for the $CoMoO_4$ sample was 2245 sec (~37 min) as compared to results reported for other $NiMoO_4$ nanofibers with reported discharge times under 500 seconds. [15] These long discharge times could be due to the analyte's level of adsorption to the substrate being higher for the oxide samples than for the sulfide samples due to the size difference between the oxide and sulfide ions. Since the charging current is observed before the capacitive double layer forms and there is no current passed as the voltage is applied, the long charging time indicates a high level of adsorption on the electrode. The impact of current density on specific capacitance was also plotted (Figure 9b) and the results were very similar to the capacitance values from Equation 3.1 except that the $NiMoO_4$ electrode performed the best at most current densities instead of the $CoMoO_4$ electrode. The CoMoP sample (Figure 10e) had a much longer cycle time than the NiMoP sample (Figure 10f), indicating a greater capacity for energy storage in the cobalt sample. Both figures show a typical pseudocapacitive shape between a rectangle and a triangle, indicating the hybrid nature of these materials. This suggests that at low current densities, at least the materials should have a high energy density. The specific capacitance (F/g) during the CD tests was calculated using Equation 3.2,

$$C_{sp} = \frac{i * \Delta t}{\Delta V * m} \tag{3.2}$$

where i is the current density (A/g), Δt is the discharge time (s), ΔV is the potential range, and m is the mass of materials. The decreasing capacitance trend with increasing density also suggests strongly that redox processes are responsible for the bulk of the electrodes' capacitance. A comparison of the specific capacitance values calculated by similar methods and in the same electrolyte is summarized in Table 1.

Table 1. Comparison of the specific capacitance of supercapacitor materials.

Name	Specific Capacitance (F/g) @ CV	Specific Capacitance (F/g) @ CD	Reference
$CoMoO_4$	2075 @ 2 mV/s	2651 @ 0.5 A/g	This work
$CoMoS_4$	3550 @ 2 mV/s	1366 @ 0.5 A/g	This work
CoMoP	3508 @ 2 mV/s	1193 @ 1.0 mA/cm^2	This work
$NiMoO_4$	1676 @ 2 mV/s	2093 @ 0.75 A/g	This work
$NiMoS_4$	1171 @ 2 mV/s	641 @ 0.5 A/g	This work
NiMoP	930 @ 2 mV/s	638 @ 1.5 mA/cm^2	This work
MoO_3-$NiMoO_4$	171.3 @ 2 mV/s	204 @ 0.5 A/g	[18]
$Ni_3V_2O_8$	118 @ 5 mV/s	-	[22]
Mo-doped ZnO	-	2296 @ 1 A/g	[38]
$CrCo_2O_4$	403.2 @ 2 mV/s	231 @ 1 A/g	[39]
$MnCo_2O_4$	378.1 @ 2 mV/s	161 @ 1 A/g	[39]
$NiCo_2O_4$	407.2 @ 2 mV/s	190 @ 1 A/g	[39]
α/β-NiS	2250 @ 2 mV/s	-	[7]
β-NiS	2150 @ 2 mV/s	-	[7]
ZnO@NiO	185 @ 2 mV/s	74 @ 0.5 A/g	[14]

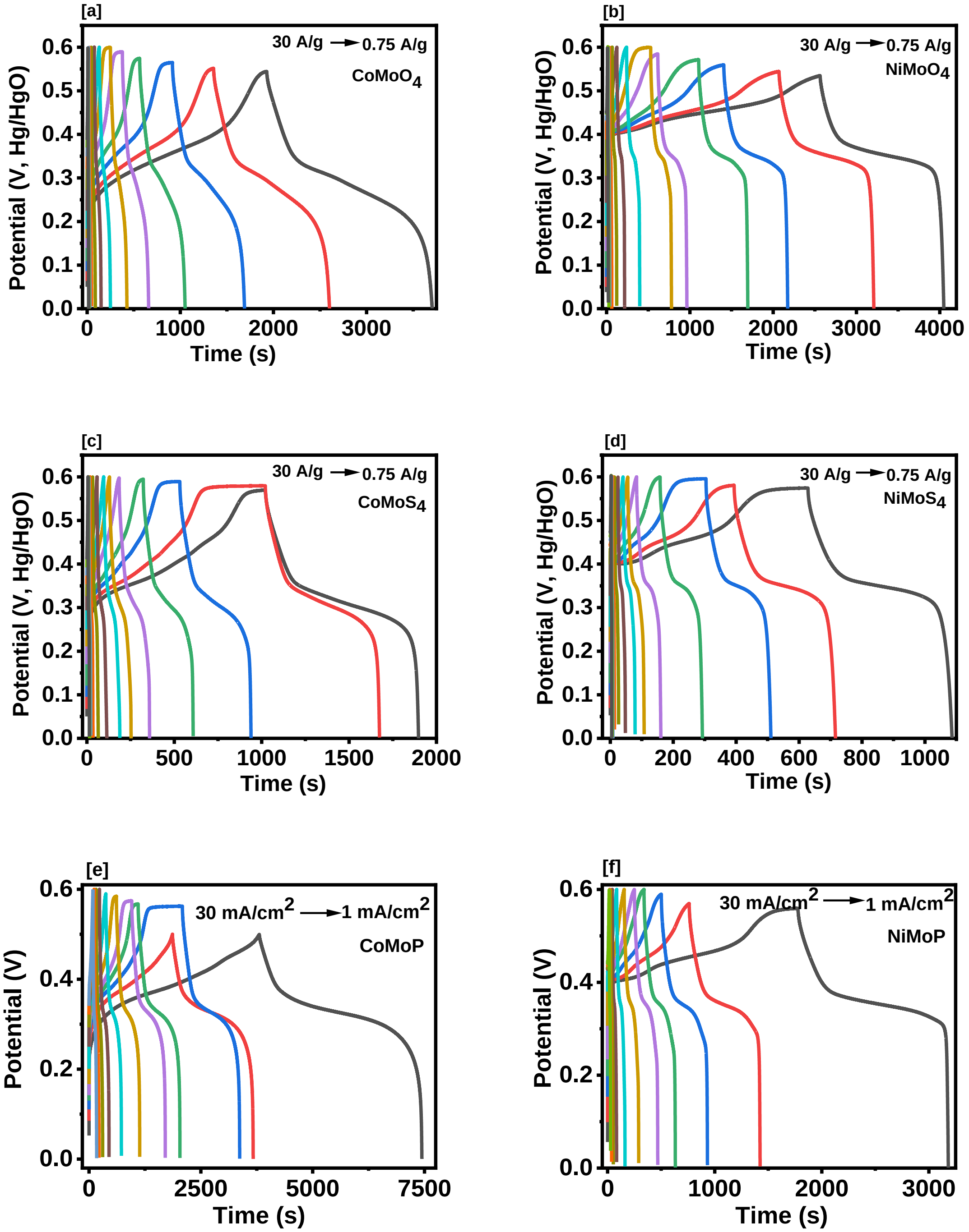

Figure 10: Potential vs time at various current densities for [a] $CoMoO_4$, [b] $NiMoO_4$, [c] $CoMoS_4$, [d] $NiMoS_4$, [e] CoMoP, and [f] NiMoP.

In each figure, CoMoP is shown to have twice the capacitance of NiMoP at low scan rates. The decline in the performance of CoMoP at higher scan rates, while still superior to the NiMoP, indicates that the advantage of two oxidation states is not proportional to the scan rate/current density and, therefore, the charging mechanism of the sample becomes less pseudocapacitive as scan rate increases. In both the CV and CD figures, it seems that the charge storage mechanism at each electrode is a diffusion-controlled process, where the lower scan rates have larger capacitance values than the faster scan rates, and the lower current densities had the longest charge/discharge rates. Table 1 compares supercapacitive properties of some cobalt and nickel-based materials with our prepared materials. Another approach to establishing the capacitive effects of the electrodes was to look into the charge storage mechanism of the electrodes themselves (Equation 3.3).

Both the CV and CD data suggest that each electrode's charge storage is a diffusion-controlled process. This can be seen in Figure 9a, as the lower scan rates have higher capacitance values than the faster scan rates and that the lower current densities had the most extended charge/discharge rates. Another method to determine the capacitive effects of the electrodes was through determining the charge storage mechanism,

$$i = av^b \tag{3.3}$$

where i represents the peak current in amperes, v the scan rate in mV/s, and a and b are fitting parameters. The value for b defines the type of charge storage mechanism, where b = 0.5 defines a diffusion-limited mechanism, and b = 1 is for a capacitive mechanism. As seen in Figure 11a, a linear fit of the plots for the peak current vs. the square root of the scan rate (from 2 to 20 mV/s) gave b values of 0.54, 0.49, 0.45, and 0.53 for $CoMoO_4$, $CoMoS_4$, $NiMoO_4$, and $NiMoS_4$ respectively. This same process was applied to the phosphide samples' curves. Their slopes were impacted by scan rate before the 20 mV/s value was reached and had b values of 0.34 and 0.46 for the CoMoP and NiMoP samples, respectively.

After the charge storage mechanism is determined, the amount of capacitance contributed to the overall total from each mechanism can be determined through the following relationship in Equation 3.4,

$$C_{sp} = k_1 + k_2 v^{-1/2} \tag{3.4}$$

using a linear plot of Equation 3.4, k_1 and k_2 values can be determined from the y-intercept and the slope of the line. The capacitive contribution is k_2 and is represented by the slope of the line, and the diffusive contribution is k_1, which is represented by the intercept. The capacitive contribution from the redox portion of the CV curve for CoMoP is 0.0014, and for NiMoP, it is 0.06448. This confirms that the charge storage mechanism [18] is largely diffusion controlled.

The Ragone plot in Figure 11b compares the four synthesized electrodes. The energy densities (E) and power densities (P) were calculated using the following equations, [40]

$$E = \frac{1}{2} C V^2 \tag{3.5}$$

$$P = \frac{E}{t} \tag{3.6}$$

where C is the specific capacitance of the active material, V is the cell potential, and t is the discharge time measured in seconds. The Ragone plot helps visualize that the $NiMoO_4$ electrode would make good supercapacitor material with a higher energy density and power density than the other four options. The energy density values for the $CoMoO_4$, $CoMoS_4$, $NiMoO_4$, and $NiMoS_4$ electrodes were calculated at 0.5 A/g and found to be 88.8, 42.0, 76.2, and 26.4 Wh/kg, respectively. The CoMoP sample has a much higher energy density and comparable power density to the NiMoP sample at all current densities. Each material's peak energy density yielded superior performance compared to other electrodes also made of transition metal oxides [39]. The power density of each electrode at 30 A/g also resulted in very promising values of 7545, 3740, 7228, and 4306 W/kg when compared to an electrode made of $AgBiS_2$ at 3600 W/kg [41, 42].

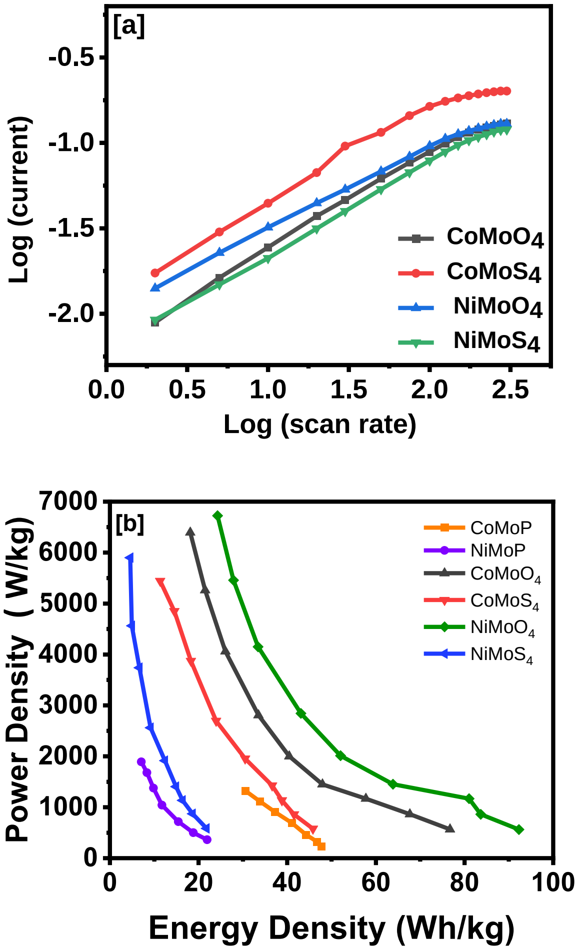

Figure 11: [a] Log (scan rate) vs. Log (current) curves and [b] Ragone plot of energy density vs. power density of synthesized samples.

Stability data for Coulombic efficiency and capacitance retention were collected for each sample over 5000 charge-discharge cycles, as shown in Figure 12. The capacitance retention of the electrode is calculated using the following equation,

$$Capacitance\ Retention = \frac{C_{sp}}{C_{spi}} \times 100\% \tag{3.7}$$

where C_{sp} is the capacitance at that cycle calculated using Equation 3.2, and C_{spi} is the initial capacitance calculated after the first cycle. The capacitance is calculated every 500 cycles and then plotted with the coulombic efficiency. Coulombic efficiency is calculated using the charge and discharge times as shown in the following equation,

$$Coulombic\ Efficiency = \frac{t_4 - t_3}{t_2 - t_1} \times 100\% \tag{3.8}$$

where t_3 and t_4 are the starting and ending times of the discharge cycle and t_1 and t_2 are the starting and ending times of the charging cycle.

The $NiMoS_4$ sample showed the most consistent Coulombic efficiency values (Figure 12d), and the $NiMoO_4$ (Figure 12b) had the least consistent Coulombic efficiency values over all cycles, but all samples stayed within a high-efficiency range of 90-100%. The $CoMoO_4$ (Figure 12a) electrode exhibited a steady decline in capacitance retention to a final value of 81%, while the $CoMoS_4$ (Figure 12c) retention value dropped sharply at first and then began to show a much steadier decline around cycle 1000 eventually falling to a retention rate of 48%. The $NiMoO_4$ sample capacitance retention fell sharply and had two slight upticks in retention around cycles 2000 and 4000, with a value of 62% after 5000 cycles. The retention for the $NiMoS_4$ fell rapidly for the first 2000 cycles and then began to rise again, ending at a value of 86% retention steadily. Further, the cyclic performance of CoMoP (Figure 12e) and NiMoP (Figure 12f) samples were tested through 5000 charge/discharge cycles. The Coulombic efficiency remained excellent with very little change for either sample through all cycles. However, the retention was seen to drop by more than 40% for each sample. Both samples seemed to lose a bit of mass during the testing, as noted by the appearance of black particulates falling to the bottom of the test beaker. This problem requires further testing of the synthesis method to improve the long-term stability of the electrodes.

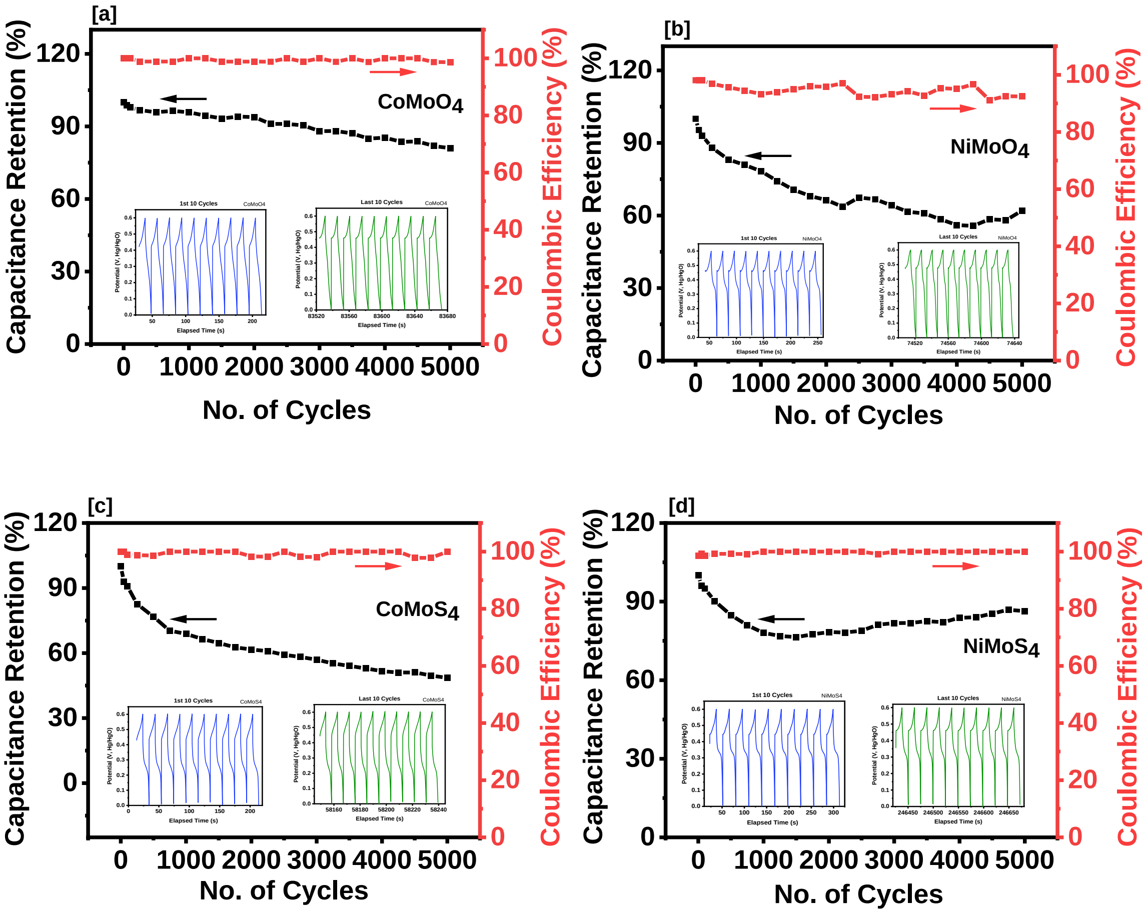

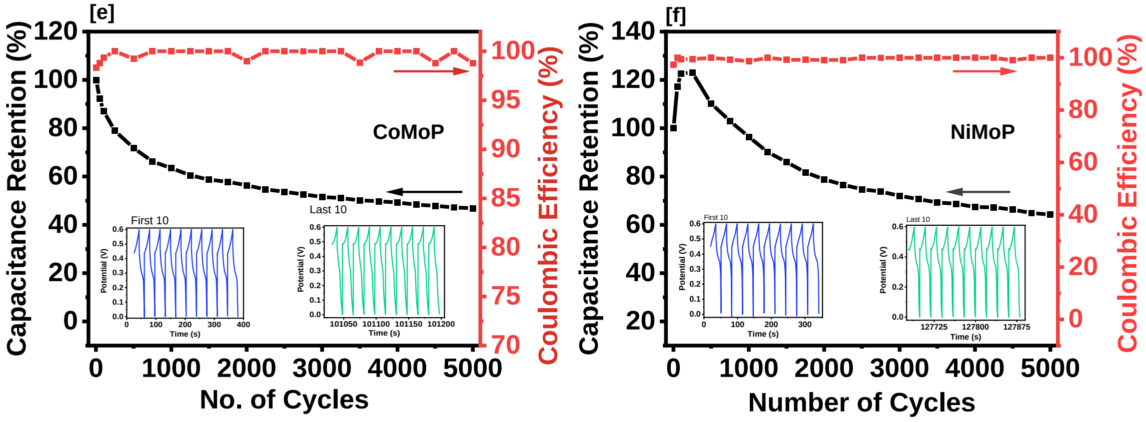

Figure 12: Capacitance rentention and coulombic efficiency for [a] CoMoO$_4$, [b] NiMoO$_4$, [c] CoMoS$_4$, [d] NiMoS$_4$, [e] CoMoP, and [f] NiMoP.

3.2.2. Electrocatalysts for water-splitting

The electrodes' electrocatalytic ability to perform hydrogen evolution reactions was also tested using the same three-electrode system in a 1 M KOH solution. The HER polarization curves for each sample were obtained after linear sweep voltammetry scans and can be seen in Figure 13a & b. The NiMoS$_4$ had the lowest overpotential of 148 mV, which was recorded at 10 mA/cm^2. At the same current density, the NiMoO$_4$ sample has the highest overpotential at 238 mV, which gives a range of overpotentials of 90 mV for all four samples. After phosphorization, the overpotential drops from 238 mV (NiMoO$_4$) and 221 mV (CoMoO$_4$) to 144 mV (NiMoP) and 137 mV, respectively to the much lower 144 (NiMoP) and 137 mV (CoMoP). The two Co-containing samples had very similar overpotentials indicating that the presence of Co was more conducive to the HER process than whether the sample was an oxide or sulfide. This does not seem to be the case with the Ni-containing samples, which show the sulfide and oxide samples as having the highest and lowest values.

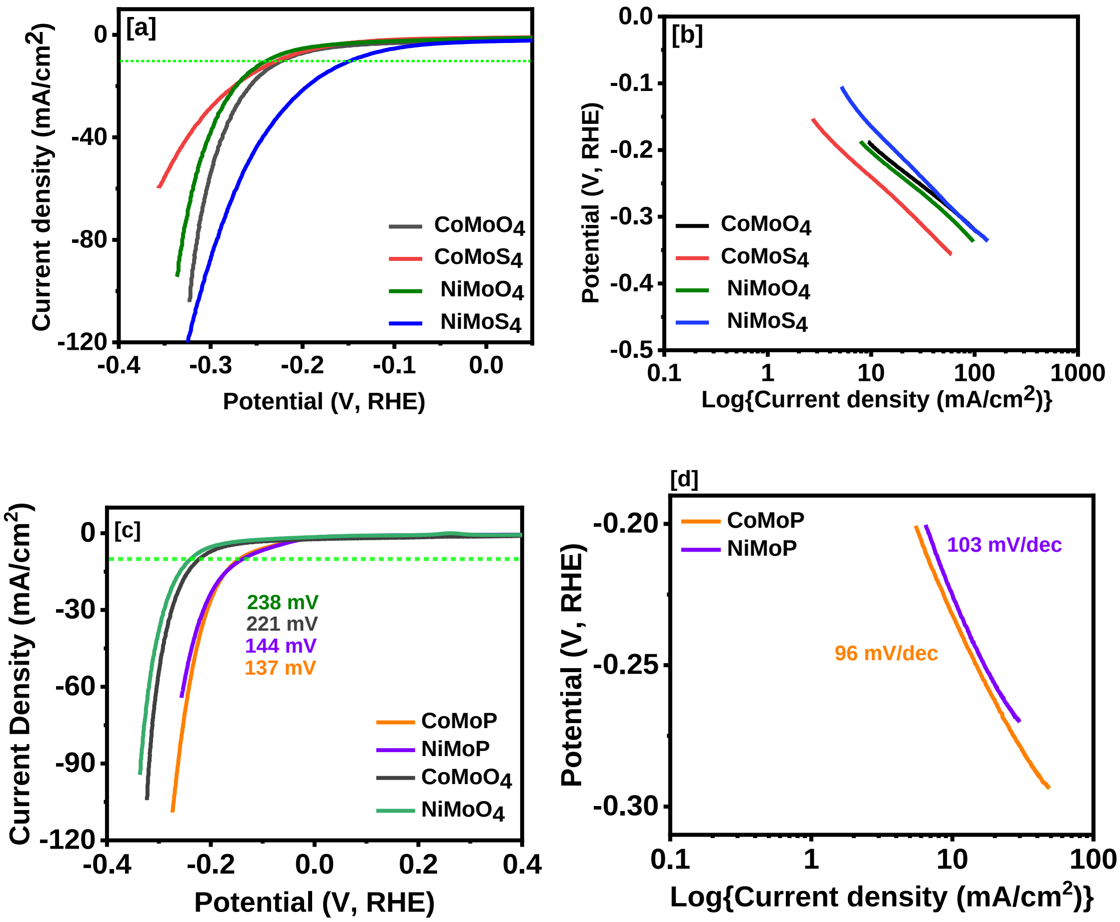

Figure 13: HER values for overpotential comparison [a] and Tafel slopes [b] of oxides and sulfides, overpotential value comparison [c] of oxides and phosphides, and Tafel slopes [d] of phosphides.

The Tafel slopes for the HER reaction are shown in Figure 13c. These results are all very similar, running from 125 to 159 mV/dec for all samples. This suggests that the reaction kinetics for hydrogen generation does not vary much based on the electrode material. The differences between the slope values in the HER and OER processes may have more to do with the level of adsorption of the gases on the electrode than on the reaction kinetics of the electrocatalytic material. The hydrogen gas produces smaller bubbles than the oxygen gas, leaving more reaction sites open and thus allowing for more contact with the electrolyte. A comparison of overpotentials and Tafel slope values may be found in Table 2. (OER values are the lowest reached overpotential at 10 mA/cm^2 on the entire CV.) Figure 13c shows the Tafel slopes for the HER on CoMoP and NiMoP catalysts. Both samples showed quite comparable Tafel slopes, indicating that their HER kinetics are very similar. The phosphide samples outperformed oxide samples, which had Tafel slopes of 125 mV (CoMoO) and 147 mV/s (NiMoO), respectively.

Table 2: Comparison of the electrocatalytic activities of materials in 1M KOH media.

Sample Name	HER η_{10} (mV)	HER Tafel Slope (mV/dec)	OER η_{10} (mV)	OER Tafel Slope (mV/dec)	Reference
$CoMoO_4$	221	125	203	98	This work
$CoMoS_4$	227	147	189	78	This work
CoMoP	137	96	387	116	This work
$NiMoO_4$	238	147	211	91	This work
$NiMoS_4$	148	159	226	54	This work
NiMoP	144	103	384	103	This work
$NiCo_2O_4$	196	135	379	75	[11]
$NiCo_2S_4$	308	133	282	99	[11]
Co-NiS	156	98	339	70	[12]
Cu-NiS	154	114	354	97	[12]
$CuCo_2O_4$	168	112	136	46	[43]
Co/Co_2P	295	80	162	60	[44]
$Co_{0.9}S_{0.58}P_{0.42}$	141	72	266	48	[45]

In addition, to test their stability, the HER polarization curves for the catalysts were recorded before and after 50 cycles as shown in Figure 14. The LSV and LSV-50 graphs compare data for the first and the 50th cycle and show no substantial loss in current density as the voltage is increased. The two sulfide samples have the best overall results, while the oxide samples show the greatest improvement between the two curves from the LSV to the LSV-50 cycles. This suggests greater stability in the sulfide electrodes for electrocatalysis than the oxide-containing samples but that the oxide samples have a significant improvement in performance over time. The $CoMoO_4$ and $NiMoO_4$ electrodes' improvement could be due to the exfoliation of the nanostructures as the gases are formed and released, giving rise to a greater active surface area for the electrode. There was no substantial decrease in current density after 50 cycles in either case for the phosphide samples, according to the data (Figure 14 e & f). The increased activity of the CoMoP and NiMoP electrodes might be ascribed to the exfoliation of the nanostructures as the gases form and release, resulting in a larger active surface area for the electrode and, as a consequence, a lower voltage required to produce the same current density as before.

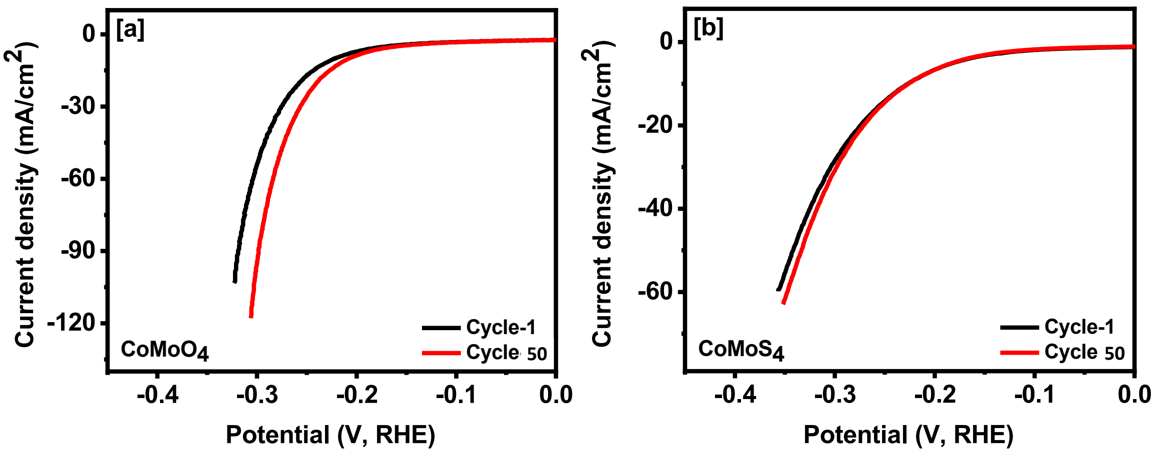

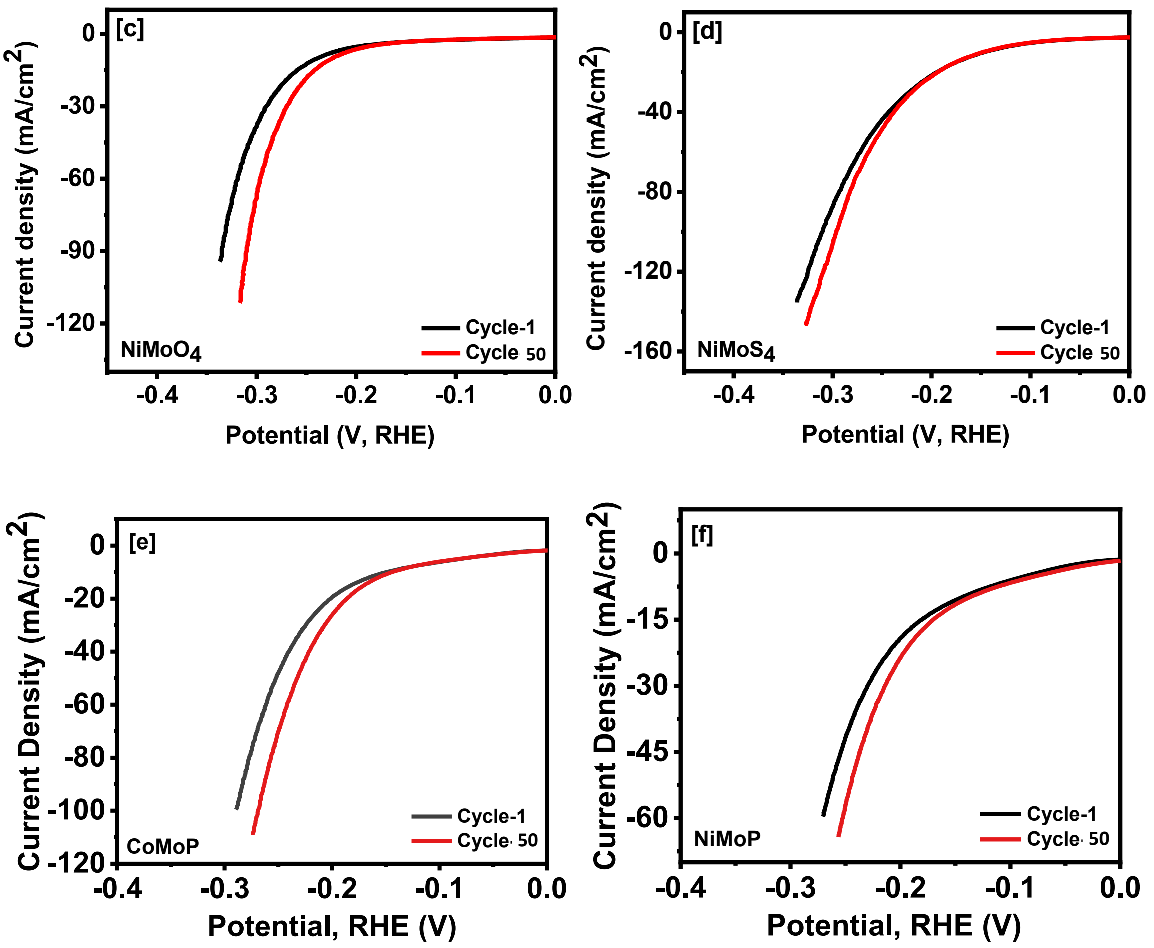

Figure 14: HER LSV plots for the first and 50th cycles of [a] $CoMoO_4$, [b] $CoMoS_4$, [c] $NiMoO_4$, [d] $NiMoS_4$, [e] CoMoP, and [f] NiMoP.

Each of the samples was tested as an electrocatalyst for oxygen evolution through linear sweep voltammetry in 1 M KOH. The polarization curves for the samples are shown in Figure 15a & b. The $CoMoS_4$ sample had the lowest overpotential of 189 mV at a current density of 10 mA/cm^2. This value is lower than the overpotential for the $NiMoS_4$ sample by 37 mV, which had the highest overpotential of all the samples. These values are comparable to nanosheet electrodes made of $CuCo_2O_4$ (136 mV) and tested in the presence of urea [46]. With the exception of the phosphorized samples which both had overpotentials greater than 380 mV, both the other Co samples have the lower of the four overpotentials, and the Ni-containing samples have the highest overpotentials. This could be due to the difference in conductivity between Ni and Co due to the size of the bandgap for each of these metals. While phosphorization seemed to have decreased the performance of the electrocatalysts for OER applications in both cases, instead of improving the process.

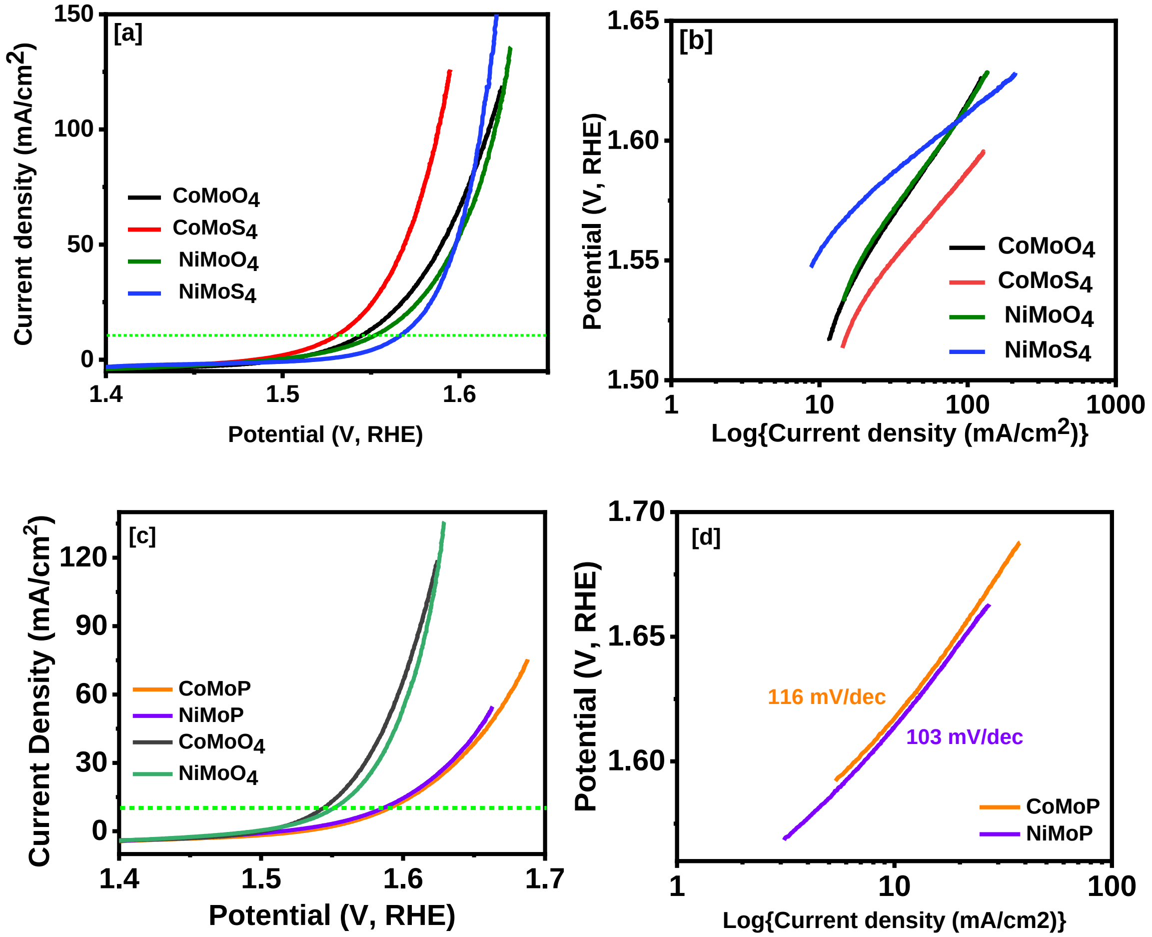

Figure 15: OER overpotential value comparison [a] and Tafel slopes [b] of oxide and sulfide samples, overpotential value comparison [c] of oxide and phosphide samples, and [d] Tafel slopes of phosphide samples.

The kinetics of the oxygen evolution reaction can be inferred from the Tafel slopes for each of the samples, as seen in Figure 15c. In this case, both of the sulfide-containing samples had the lower values, with $NiMoS_4$ being the lowest at 54 mV/dec. Both oxide-containing samples had very similar results, with 91 mV/dec for the $NiMoO_4$ and 98 mV/dec for the $CoMoO_4$. "The low Tafel slope value...indicates faster OER kinetics and can be correlated to the high electrocatalytic surface area of the electrodeposited Ni-foam electrode [10]." This is of note since the oxygen gases formed during the OER process are larger than the hydrogen gases formed in the HER process, so the surface morphology of the electrode becomes very important as the oxygen gas was much less likely to become trapped in the amorphous surface of the $NiMoS_4$ (compare Figure 3b & d). The similar Tafel values for $CoMoO_4$ (98 mV/dec) and $NiMoO_4$ (91 mV/dec) show no significant difference in the reaction kinetics of the two electrodes and therefore not a substantial benefit in using one material over the other for OER. The tafel slopes for the phosphide samples are much higher values, indicating a much slower reaction than the oxide and sulfide electrocatalysts. The phosphide samples tafel slopes also show no substantial difference in value when comparing CoMoP (116 mV/dec) and NiMoP (103 mV/dec), which also indicates that neither material has any greater benefit for OER than the oxide samples.

The electrochemical impedance spectroscopy results (Figure 16) agree with the recorded overpotentials in that the Ni-containing samples have a larger charge transfer resistance and, therefore a higher overpotential than the Co-containing samples. Therefore, the Co-containing samples could provide better catalytic performance than the Ni samples. The total resistance was analyzed from voltages of 0.45 to 0.6 V (V, SCE). The EIS data show a consistent trend in decreasing impedance as the applied potential values are increased. The Nyquist plots for the samples also shows a charge transfer resistance (R_{ct}) of 1.1214, 0.7062, 1.4686, and 0.90457 (Ohms/cm^2) for $CoMoO_4$, $CoMoS_4$, $NiMoO_4$, and

$NiMoS_4$ respectively at 0.6 V (V, SCE). This finding suggests that this $NiMoS_4$ electrode responded to the applied higher voltage with more resonance than the other samples. At low potentials, the R_{ct} value is impacted more by the inductance and the capacitance of the system than the real impedance due to the electrode material. This relationship holds for all six materials, displaying that more catalytic activity can happen when the potential value is higher. However, the phosphide materials had much larger R_{ct} values as can be clearly seen in the graph, which suggests a reason why their OER overpotential values were higher than the other samples.

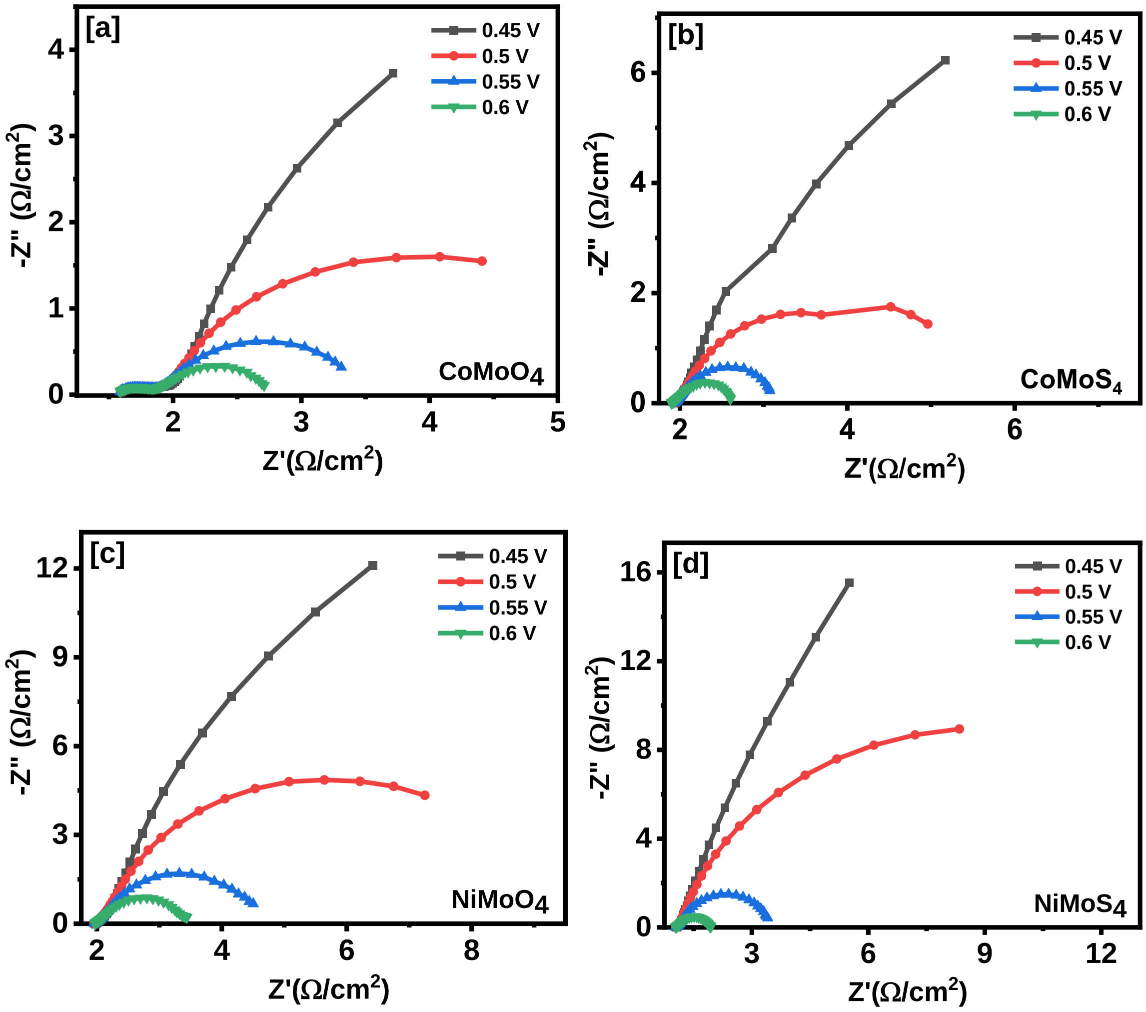

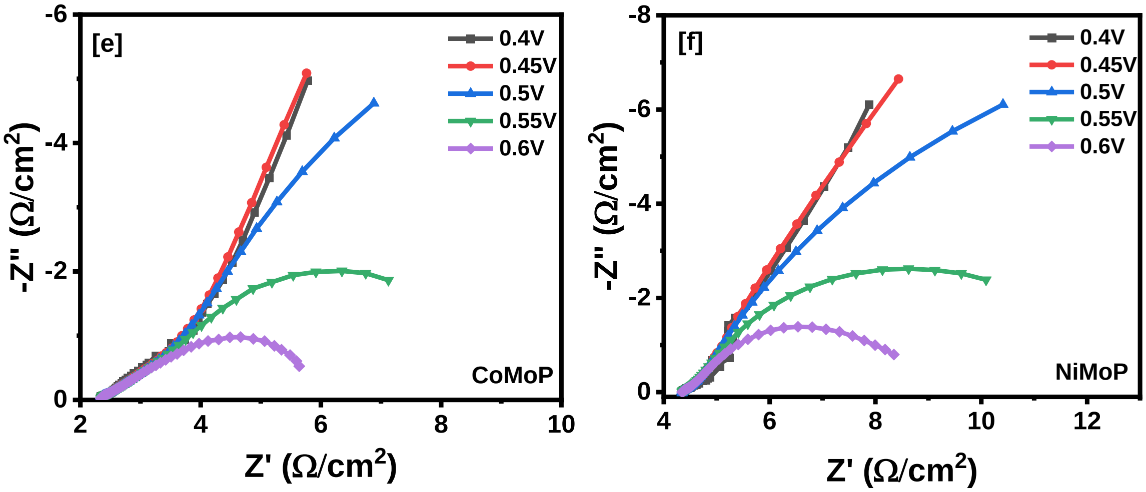

Figure 16: EIS graphs for [a] $CoMoO_4$, [b] $CoMoS_4$, [c] $NiMoO_4$, and [d] $NiMoS_4$, [e] CoMoP, and [f] NiMoP.

The stability of the samples was tested by comparing the polarization curves for the first cycle and the 50th cycle and through chronoamperometry (Figure 17). The LSV data shows the least change in the potential to achieve the same current density for the Co-containing samples and the greatest for the Ni-containing samples. This can be seen by the difference in area between the two curves (Figure 17 a – f). Chronoamperometry data collected at a constant voltage over 18 hours suggests that the $CoMoO_4$ sample had the smallest noticeable change in current density of approximately 3 mA/cm^2. The other samples saw decreases in approximately 5, 7, & 10 mA/cm^2 for the $NiMoS_4$, $CoMoS_4$, & $NiMoO_4$, respectively. While the phosphide samples saw no perceptible change in current density.

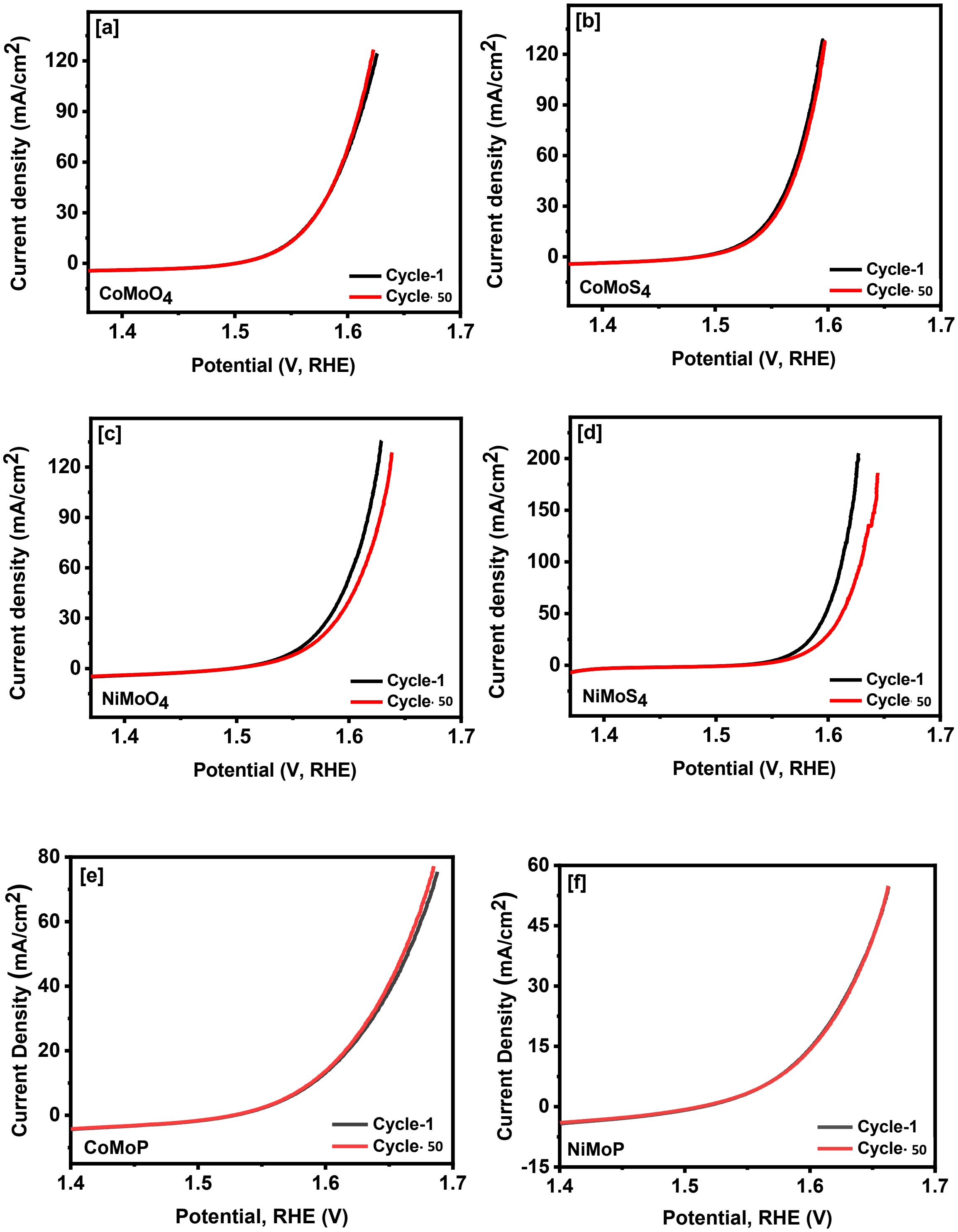
[a]
CoMoO4
Cycle-1
Cycle- 50
Current density (mA/cm2)
120
90
60
30
0
1.4
1.5
1.6
1.7
Potential (V, RHE)
[b]
CoMoS4
Cycle-1
Cycle- 50
Current density (mA/cm2)
120
90
60
30
0
1.4
1.5
1.6
1.7
Potential (V, RHE)
[c]
NiMoO4
Cycle-1
Cycle- 50
Current density (mA/cm2)
120
90
60
30
0
1.4
1.5
1.6
1.7
Potential (V, RHE)
[d]
NiMoS4
Cycle-1
Cycle- 50
Current density (mA/cm2)
200
150
100
50
0
1.4
1.5
1.6
1.7
Potential (V, RHE)
[e]
CoMoP
Cycle-1
Cycle- 50
Current Density (mA/cm2)
80
60
40
20
0
1.4
1.5
1.6
1.7
Potential, RHE (V)
[f]
NiMoP
Cycle-1
Cycle- 50
Current Density (mA/cm2)
60
45
30
15
0
-15
1.4
1.5
1.6
1.7
Potential, RHE (V)

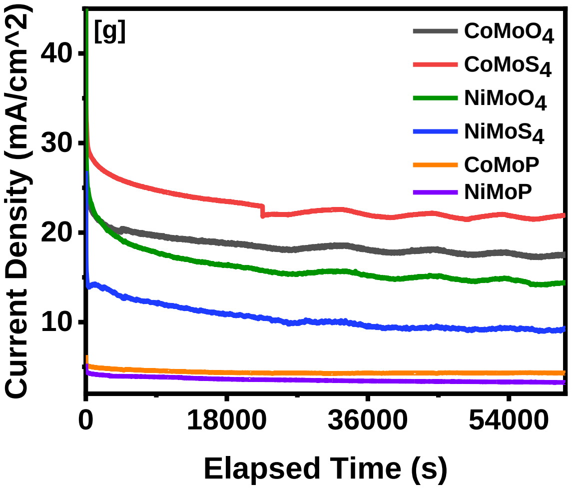

Figure 17: Stability performance using LSV measurements at 1st and 50th cycles [a-f], and chronoamperometry test [g].

CHAPTER IV

CONCLUSIONS

In conclusion, nanoflower sheets of $CoMoO_4$, $CoMoS_4$, and CoMoP and nanowires of $NiMoO_4$, $NiMoS_4$, and NiMoP structures were synthesized on nickel foam through a facile hydrothermal method to be used as energy storage and conversion device. These nanostructures displayed defined shapes as oxides and limited crystalline structures as sulfides and phoshides. The $CoMoS_4$ electrode exhibited the best energy storage capability with a specific capacitance of 3551 F/g at 2 mV/s, good stability after 5000 cycles, and an average Coulombic Efficiency of 99% across all cycles. For HER purposes, the CoMoP electrode yielded the lowest overpotential at 137 mV and stable current density after 1000 cycles. The electrode with the best OER results was the $CoMoS_4$ nanostructure. It exhibited an overpotential of 189 mV and a lower charge transfer resistance than either oxide-containing electrode. These results point to the potential of multifunctional and cost-effective use of electrode materials for energy storage and generation.

References

1. Jiang P, Fan Y Van, Klemeš JJ (2021) Impacts of COVID-19 on energy demand and consumption: Challenges, lessons and emerging opportunities. Appl Energy 285:116441

2. Ruan G, Wu D, Zheng X, Zhong H, Kang C, Dahleh MA, Sivaranjani S, Xie L (2020) A Cross-Domain Approach to Analyzing the Short-Run Impact of COVID-19 on the US Electricity Sector. Joule 4:2322–2337

3. Solheim JE, Stordahl K, Humlum O (2012) The long sunspot cycle 23 predicts a significant temperature decrease in cycle 24. J Atmos Solar-Terrestrial Phys 80:267–284

4. Huang J, Hitchcock P, Maycock AC, McKenna CM, Tian W (2021) Northern hemisphere cold air outbreaks are more likely to be severe during weak polar vortex conditions. Commun Earth Environ 2021 21 2:1–11

5. Winter M, Brodd RJ (2004) What are batteries, fuel cells, and supercapacitors? Chem Rev 104:4245–4269

6. Kularatna N, Gunawardane K (2021) New developments of larger supercapacitors: Symmetrical devices, hybrid types, and battery-capacitors. Energy Storage Devices Renew Energy-Based Syst 239–249

7. Shombe GB, Khan MD, Zequine C, Zhao C, Gupta RK, Revaprasadu N (2020) Direct solvent free synthesis of bare α-NiS, β-NiS and α-β-NiS composite as excellent electrocatalysts: Effect of self-capping on supercapacitance and overall water splitting activity. Sci Rep 10:1–14

8. Khan MD, Awan SU, Zequine C, Zhang C, Gupta RK, Revaprasadu N (2020)

Controlled Synthesis of Sb2(S1- xSex)3 (0 ≤ x ≤ 1) Solid Solution and the Effect of Composition Variation on Electrocatalytic Energy Conversion and Storage. ACS Appl Energy Mater 3:1448–1460

9. Thompson K, Choi J, Neupane D, Mishra SR, Perez F, Gupta RK (2021) Tuning the electrochemical properties of nanostructured CoMoO4 and NiMoO4 via a facile sulfurization process for overall water splitting and supercapacitors. Surf Coatings Technol 421:127435
10. Zhang C, Bhoyate S, Zhao C, Kahol PK, Kostoglou N, Mitterer C, Hinder SJ, Baker MA, Constantinides G, Polychronopoulou K, Rebholz C, Gupta RK (2019) Electrodeposited nanostructured CoFe 2 O 4 for overall water splitting and supercapacitor applications. Catalysts 9:176
11. Ndambakuwa W, Ndambakuwa Y, Choi J, Fernando G, Neupane D, Mishra SR, Perez F, Gupta RK (2021) Nanostructured nickel-cobalt oxide and sulfide for applications in supercapacitors and green energy production using waste water. Surf Coatings Technol 410:126933
12. Shombe GB, Khan MD, Alenad AM, Choi J, Ingsel T, Gupta RK, Revaprasadu N (2020) Unusual doping induced phase transitions in NiSviasolventless synthesis enabling superior bifunctional electrocatalytic activity. Sustain Energy Fuels 4:5132–5143
13. Naito T, Shinagawa T, Nishimoto T, Takanabe K (2021) Recent advances in understanding oxygen evolution reaction mechanisms over iridium oxide. Inorg Chem Front 8:2900–2917
14. Shaheen I, Ahmad KS, Zequine C, Gupta RK, Thomas AG, Malik MA (2020)

Effect of NiO on organic framework functionalized ZnO nanoparticles for energy storage application. Int J Energy Res 44:5259–5271

15. Thiagarajan K, Bavani T, Arunachalam P, Lee SJ, Theerthagiri J, Madhavan J, Pollet BG, Choi MY (2020) Nanofiber NiMoO4/g-C3N4 composite electrode materials for redox supercapacitor applications. Nanomaterials 10:1–14
16. Liu MC, Kong L Bin, Lu C, Ma XJ, Li XM, Luo YC, Kang L (2013) Design and synthesis of CoMoO4-NiMoO4·xH 2O bundles with improved electrochemical properties for supercapacitors. J Mater Chem A 1:1380–1387
17. Yang Q, Lin SY (2016) Rationally designed nanosheet-based CoMoO4-NiMoO4 nanotubes for high-performance electrochemical electrodes. RSC Adv 6:10520–10526
18. Shaheen I, Ahmad KS, Zequine C, Gupta RK, Thomas AG, Malik MA (2020) Functionalization of MoO3[sbnd]NiMoO4 nanocomposite using organic template for energy storage application. J Energy Storage 29:101309
19. Theerthagiri J, Senthil RA, Buraidah MH, Madhavan J, Arof AK, Ashokkumar M (2016) One-step electrochemical deposition of Ni1-xMoxS ternary sulfides as an efficient counter electrode for dye-sensitized solar cells. J Mater Chem A 4:16119–16127
20. Lv Z, Zhong Q, Zhao Z, Bu Y (2017) Facile synthesis of hierarchical nickel–cobalt sulfide quadrangular microtubes and its application in hybrid supercapacitors. J Mater Sci Mater Electron 28:18064–18074
21. Anantharaj S, Ede SR, Sakthikumar K, Karthick K, Mishra S, Kundu S (2016) Recent Trends and Perspectives in Electrochemical Water Splitting with an

Emphasis on Sulfide, Selenide, and Phosphide Catalysts of Fe, Co, and Ni: A Review. ACS Catal. 6:8069–8097

22. Thiagarajan K, Theerthagiri J, Senthil RA, Arunachalam P, Madhavan J, Ghanem MA (2018) Synthesis of Ni3V2O8@graphene oxide nanocomposite as an efficient electrode material for supercapacitor applications. J Solid State Electrochem 22:527–536
23. Bhoyate S, Kahol PK, Sapkota B, Mishra SR, Perez F, Gupta RK (2018) Polystyrene activated linear tube carbon nanofiber for durable and high-performance supercapacitors. Surf Coatings Technol 345:113–122
24. Guo G, Song Z, Cong C, Zhang K (2007) CoMoS4 nanoflowers as anode for secondary lithium batteries. J Nanoparticle Res 9:653–656
25. Shao L, Qian X, Wang X, Li H, Yan R, Hou L (2016) Low-cost and highly efficient CoMoS4/NiMoS4-based electrocatalysts for hydrogen evolution reactions over a wide pH range. Electrochim Acta 213:236–243
26. Zell T, Langer R (2016) Iron-catalyzed hydrogenation and dehydrogenation reactions with relevance to reversible hydrogen storage applications. Recycl Catal 2:87–109
27. Chung HT (2020) High-Performance Ultralow-Cost Non- Precious Metal Catalyst System for AEM Electrolyzer. 2020 DOE Annu Merit Rev - Proj ID p185 1–5
28. Li B, Jiang L, Li X, Ran P, Zuo P, Wang A, Qu L, Zhao Y, Cheng Z, Lu Y (2017) Preparation of Monolayer MoS2 Quantum Dots using Temporally Shaped Femtosecond Laser Ablation of Bulk MoS2 Targets in Water. Sci Reports 2017 71 7:1–12

29. Tan BJ, Klabunde KJ, Sherwood PMA (1991) XPS Studies of Solvated Metal Atom Dispersed Catalysts. Evidence for Layered Cobalt—Manganese Particles on Alumina and Silica. J Am Chem Soc 113:855–861

30. Kasztelan S, Grimblot J, Bonnelle JP, Payen E, Toulhoat H, Jacquin Y (1983) Preparation of Co-Mo-γAl2O3 and Ni-Mo-γAl2O3 catalysts by ph regulation of molybdenum solution. characterization of supported species and hydrogenation activities. Appl Catal 7:91–112

31. Korányi TI, Manninger I, Paál Z, Marks O, Günter JR (1989) Activation of unsupported CoMo catalysts in thiophene hydrodesulfurization. J Catal 116:422–439

32. Alstrup I, Chorkendorff I, Candia R, Clausen BS, Topsøe H (1982) A combined X-Ray photoelectron and Mössbauer emission spectroscopy study of the state of cobalt in sulfided, supported, and unsupported CoMo catalysts. J Catal 77:397–409

33. Biesinger MC, Lau LWM, Gerson AR, Smart RSC (2012) The role of the Auger parameter in XPS studies of nickel metal, halides and oxides. Phys Chem Chem Phys 14:2434–2442

34. Wu H, Lian K (2014) The Development of Pseudocapacitive Molybdenum Oxynitride Electrodes for Supercapacitors. ECS Trans 58:67–75

35. Cao P, Peng J, Liu S, Cui Y, Hu Y, Chen B, Li J, Zhai M (2017) Tuning the Composition and Structure of Amorphous Molybdenum Sulfide/Carbon Black Nanocomposites by Radiation Technique for Highly Efficient Hydrogen Evolution. Sci Rep 7:1–11

36. Yang D, Yang L, Zhong L, Yu X, Feng L (2019) Urea electro-oxidation efficiently

catalyzed by nickel-molybdenum oxide nanorods. Electrochim Acta 295:524–531

37. Lou BS, Rajaji U, Chen SM, Chen TW (2020) A simple sonochemical assisted synthesis of NiMoO4/chitosan nanocomposite for electrochemical sensing of amlodipine in pharmaceutical and serum samples. Ultrason Sonochem 64:104827

38. Ali A, Ammar M, Ali M, Yahya Z, Javaid MY, Hassan SU, Ahmed T (2019) Mo-doped ZnO nanoflakes on Ni-foam for asymmetric supercapacitor applications. RSC Adv 9:27432–27438

39. Guragain D, Zequine C, Gupta RK, Mishra SR (2020) Facile synthesis of bio-template tubular MCo2O4 (M = Cr, Mn, Ni) microstructure and its electrochemical performance in aqueous electrolyte. Processes 8:1–18

40. Choi J, Zequine C, Bhoyate S, Lin W, Li X, Kahol P, Gupta R (2019) Waste Coffee Management: Deriving High-Performance Supercapacitors Using Nitrogen-Doped Coffee-Derived Carbon. C 2019, Vol 5, Page 44 5:44

41. Colli AN, Girault HH, Battistel A (2019) Non-precious electrodes for practical alkaline water electrolysis. Materials (Basel) 12:1–17

42. Khan MD, Aamir M, Sohail M, Bhoyate S, Hyatt M, Gupta RK, Sher M, Revaprasadu N (2019) Electrochemical investigation of uncapped AgBiS2 (schapbachite) synthesized using in situ melts of xanthate precursors. Dalt Trans 48:3714–3722

43. Haque F, Zavabeti A, Zhang BY, Datta RS, Yin Y, Yi Z, Wang Y, Mahmood N, Pillai N, Syed N, Khan H, Jannat A, Wang N, Medhekar N, Kalantar-Zadeh K, Ou JZ (2019) Ordered intracrystalline pores in planar molybdenum oxide for enhanced alkaline hydrogen evolution. J Mater Chem A 7:257–268

44. Masa J, Barwe S, Andronescu C, Sinev I, Ruff A, Jayaramulu K, Elumeeva K, Konkena B, Roldan Cuenya B, Schuhmann W (2016) Low Overpotential Water Splitting Using Cobalt-Cobalt Phosphide Nanoparticles Supported on Nickel Foam. ACS Energy Lett 1:1192–1198

45. Dai Z, Geng H, Wang J, Luo Y, Li B, Zong Y, Yang J, Guo Y, Zheng Y, Wang X, Yan Q (2017) Hexagonal-Phase Cobalt Monophosphosulfide for Highly Efficient Overall Water Splitting. ACS Nano 11:11031–11040

46. Zequine C, Wang F, Li X, Guragain D, Mishra SR, Siam K, Kahol PK, Gupta RK (2019) Nanosheets of CuCo 2 O 4 as a high-performance electrocatalyst in urea oxidation. Appl Sci 9:793